

GAMA/WiggleZ: the 1.4 GHz radio luminosity functions of high- and low-excitation radio galaxies and their redshift evolution to $z = 0.75$

Michael B. Pracy,^{1*} John H. Y. Ching,¹ Elaine M. Sadler,¹ Scott M. Croom,¹
I. K. Baldry,² Joss Bland-Hawthorn,¹ S. Brough,³ M. J. I. Brown,⁴ Warrick J. Couch,³
Tamara M. Davis,⁵ Michael J. Drinkwater,⁵ A. M. Hopkins,³ M. J. Jarvis,^{6,7}
Ben Jelliffe,¹ Russell J. Jurek,⁸ J. Loveday,⁹ K. A. Pimblet,^{10,11} M. Prescott,⁷
Emily Wisnioski¹² and David Woods¹³

¹*Sydney Institute for Astronomy, School of Physics, University of Sydney, NSW 2006, Australia*

²*Astrophysics Research Institute, Liverpool John Moores University, IC2, Liverpool Science Park, 146 Brownlow Hill, Liverpool L3 5RF, UK*

³*Australian Astronomical Observatory, PO Box 915, North Ryde, NSW 1670, Australia*

⁴*School of Physics and Astronomy, Monash University, Clayton, VIC 3800, Australia*

⁵*School of Mathematics and Physics, University of Queensland, Brisbane, QLD 4072, Australia*

⁶*Oxford Astrophysics, Department of Physics, Keble Road, Oxford OX1 3RH, UK*

⁷*Astrophysics Group, Department of Physics, University of the Western Cape, Bellville 7535, South Africa*

⁸*Australia Telescope National Facility, CSIRO, Epping, NSW 1710, Australia*

⁹*Astronomy Centre, University of Sussex, Falmer, Brighton BN1 9QH, UK*

¹⁰*E.A. Milne Centre for Astrophysics and Department of Physics and Mathematics, University of Hull, Cottingham Road, Kingston-upon-Hull HU6 7RX, UK*

¹¹*School of Physics, Monash University, Clayton, VIC 3800, Australia*

¹²*Max Planck Institut für extraterrestrische Physik, Giessenbachstraße, D-85748 Garching, Germany*

¹³*Department of Physics and Astronomy, University of British Columbia, 6224 Agricultural Road, Vancouver, BC V6T 1Z1, Canada*

Accepted 2016 April 15. Received 2016 April 14; in original form 2015 December 24

ABSTRACT

We present radio active galactic nuclei (AGN) luminosity functions over the redshift range $0.005 < z < 0.75$. The sample from which the luminosity functions are constructed is an optical spectroscopic survey of radio galaxies, identified from matched Faint Images of the Radio Sky at Twenty-cm survey (FIRST) sources and Sloan Digital Sky Survey images. The radio AGN are separated into low-excitation radio galaxies (LERGs) and high-excitation radio galaxies (HERGs) using the optical spectra. We derive radio luminosity functions for LERGs and HERGs separately in the three redshift bins ($0.005 < z < 0.3$, $0.3 < z < 0.5$ and $0.5 < z < 0.75$). The radio luminosity functions can be well described by a double power law. Assuming this double power-law shape the LERG population displays little or no evolution over this redshift range evolving as $\sim(1+z)^{0.06^{+0.17}_{-0.18}}$ assuming pure density evolution or $\sim(1+z)^{0.46^{+0.22}_{-0.24}}$ assuming pure luminosity evolution. In contrast, the HERG population evolves more rapidly, best fitted by $\sim(1+z)^{2.93^{+0.46}_{-0.47}}$ assuming a double power-law shape and pure density evolution. If a pure luminosity model is assumed, the best-fitting HERG evolution is parametrized by $\sim(1+z)^{7.41^{+0.79}_{-1.33}}$. The characteristic break in the radio luminosity function occurs at a significantly higher power ($\gtrsim 1$ dex) for the HERG population in comparison to the LERGs. This is consistent with the two populations representing fundamentally different accretion modes.

Key words: galaxies: active – radio continuum: galaxies.

1 INTRODUCTION

The evolution of galaxies and the supermassive black holes at their centres appear to be closely connected. This connection is evident

in the correlation between black hole mass and the stellar bulge mass (Magorrian et al. 1998) and black hole mass and stellar velocity dispersion (e.g. Gebhardt et al. 2000). One way this coupling may occur is via feedback processes from the active galactic nuclei (AGN) depositing energy, released by the accretion of matter on to the black hole, into their host galaxy and its surrounding environment. For example, radio jets from AGN are commonly invoked as

*E-mail: mpracy@gmail.com

a feedback mechanism to inhibit gas cooling and suppress star formation in massive galaxies and clusters of galaxies (e.g. Binney & Tabor 1995; Fabian et al. 2002; Best et al. 2006; Bower et al. 2006; Croton et al. 2006; McNamara & Nulsen 2007). Such a feedback cycle can simultaneously solve the cooling flow problem; the sharp bright-end turn down in the optical galaxy luminosity function and the fact that the most massive bulge-dominated galaxies contain the oldest stellar populations (Croton et al. 2006).

The properties of the AGN population indicate that there are two fundamentally different accretion modes operating (Hardcastle, Evans & Croston 2007; Best & Heckman 2012). In the classical ‘cold mode’, material is accreted on to the supermassive black hole via a small, geometrically thin, optically luminous accretion disc. This disc is the source of ionizing photons producing both broad- and narrow-line emission in the optical spectrum of AGN and X-ray emission via the inverse-Compton process. In the unified AGN model (Antonucci 1993), the broad-line region is obscured by a dusty torus when viewed from certain orientations resulting in the type I (not obscured) and type II (obscured) AGN classifications. As a result of the emission lines in their optical spectra, these ‘cold-mode’ AGN are also referred to as ‘quasar-mode’ or ‘high-excitation’ AGN. However, there is a large population of AGN observable by their radio emission but without the bright high-ionization emission lines in their optical spectra (e.g. Hine & Longair 1979; Laing et al. 1994; Jackson & Rawlings 1997; Best & Heckman 2012). These display no evidence for the presence of an accretion disc or dusty torus (e.g. Chiaberge et al. 2002; Whysong & Antonucci 2004) and are likely powered by radiatively inefficient accretion possibly from a hot gas halo (e.g. Hardcastle et al. 2007; Best & Heckman 2012). These ‘hot-mode’ AGN (also referred to as ‘radio-mode’ or ‘low-excitation’ AGN) are generally more massive, have higher mass-to-light ratios, are redder, and are of earlier morphological type than strong-lined AGN (e.g. Kauffmann et al. 2003; Kauffmann, Heckman & Best 2008; Best & Heckman 2012). The ‘cold-mode’ AGN display a higher rate of interactions and peculiarities in their morphology (e.g. Smith & Heckman 1989).

Both AGN modes will inject energy into their environment and have the potential to influence star formation and galaxy evolution. In the ‘hot mode’ the radio jets heat the surrounding hot gas atmosphere. This is the same gas that fuels the AGN allowing a self-regulating feedback cycle with a balance established between heating and cooling (Best et al. 2006; Croton et al. 2006). In the ‘cold-mode’ AGN are known to drive winds in their host galaxy (e.g. Ganguly & Brotherton 2008; Harrison et al. 2014; McElroy et al. 2015) and have been suggested as mechanisms to both enhance (Silk & Nusser 2010) and suppress (Shabala, Kaviraj & Silk 2011; Davis et al. 2012; Page et al. 2012) star formation.

In the local Universe, the number of radio AGN with low-excitation optical spectra (low-excitation radio galaxies, hereafter LERGs) outnumber the high-excitation radio galaxies (hereafter HERGs) at all but the highest radio luminosities (Best & Heckman 2012). The change in the dominant population occurs at $L_{1.4\text{GHz}} \sim 10^{26} \text{ W Hz}^{-1}$. The cosmic evolution of the space density of radio AGN is sensitive to radio luminosity. It is well established that the density of the most powerful radio AGN increases rapidly with increasing redshift out to $z \sim 2$ (Longair 1966; Doroshkevich, Longair & Zeldovich 1970; Willott et al. 2001; Sadler et al. 2007) – increasing by a factor of ~ 1000 . At higher redshift the space density flattens and then decreases. The decrease occurs at higher redshift for more luminous sources (e.g. Peacock 1985; Dunlop & Peacock 1990; Cirasuolo et al. 2006). This fast-evolving high-luminosity population is mostly associated with Fanaroff–Riley II

radio sources (Jackson & Wall 1999) and objects with strong optical emission lines (Willott et al. 2001; Best & Heckman 2012), i.e. HERGs. Conversely, the low-luminosity radio sources are more commonly associated with Fanaroff–Riley I sources and objects which lack strong optical emission lines, i.e. LERGs. The space density of these low-luminosity radio galaxies shows little (a factor of ~ 2) or no redshift evolution out to $z \sim 1$ (e.g. Clewley & Jarvis 2004; Sadler et al. 2007; Donoso, Best & Kauffmann 2009; Smolčić et al. 2009; McAlpine, Jarvis & Bonfield 2013).

Best & Heckman (2012) constructed the first radio galaxy luminosity function with the LERG and HERG contributions separated. They found, that while the LERGs outnumber the HERGs below $L_{1.4\text{GHz}} \sim 10^{26} \text{ W Hz}^{-1}$, examples of both classes are found at all radio luminosities. The HERG population shows evidence of evolution over the redshift range of their sample ($z < 0.3$), while there is no evidence for cosmic evolution of the LERG population. This implies the evolution of the radio luminosity functions dependence on radio luminosity can, at least in part, be explained by a changing mix in the populations (Best & Heckman 2012). Best et al. (2014) using a composite of eight published AGN samples (Wall & Peacock 1985; Lacy et al. 1999; Waddington et al. 2001; Hill & Rawlings 2003; Simpson et al. 2006; Gendre, Best & Wall 2010; Rigby et al. 2011) constructed a catalogue of 211 radio-loud AGN in the range $0.5 < z < 1.0$. Using this to compare with local samples (Best & Heckman 2012; Heckman & Best 2014) they made the first measurement of the evolution of the radio AGN population separated, spectroscopically, into LERGs (jet mode in their nomenclature) and HERGs (dubbed radiative mode). They found that the space density of the HERGs in their sample increased by around an order of magnitude to $z = 1$. In contrast, the LERG AGN density decreased with redshift at luminosities below $L_{1.4\text{GHz}} \sim 10^{26} \text{ W Hz}^{-1}$ and increased at higher luminosities.

In this paper, we present the radio luminosity function of LERGs and HERGs and their cosmic evolution to $z = 0.75$, corresponding to the second half of the history of the Universe. These luminosity functions are based on a new sample of over 5000 radio galaxies ($0.005 < z < 0.75$) with confirmed spectroscopic redshifts and spectroscopic classifications. Throughout this paper, we convert from observed to physical units assuming a $\Omega_M = 0.3$, $\Omega_\Lambda = 0.7$ and $H_0 = 70 \text{ km s}^{-1} \text{ Mpc}^{-1}$ cosmology.

2 SAMPLE CONSTRUCTION

The underlying sample from which we constructed the luminosity distributions of various radio galaxy populations is the Large Area Radio Galaxy Evolution Spectroscopic Survey (Ching 2015). This sample was constructed by matching the Faint Images of the Radio Sky at Twenty-cm survey (FIRST; Becker, White & Helfand 1995) with the photometric catalogue of the Sloan Digital Sky Survey data release 6 (SDSS; Adelman-McCarthy et al. 2008). The catalogues were matched to all objects in the FIRST catalogue ($\lesssim 0.5 \text{ mJy}$) and an optical apparent magnitude limit of $i = 20.5$ (SDSS i -band model magnitudes). The matching procedure was designed to include both point and extended radio sources, including those with multiple components. This matching was performed over $\sim 900 \text{ deg}^2$ of sky in regions where a high completeness of optical spectroscopy could be obtained. A careful estimation of the matching reliability and completeness was performed by Ching (2015) using Monte Carlo simulations of randomized catalogues. The overall reliability of the matching is estimated as ~ 93.5 per cent and the overall completeness is ~ 95 per cent. The incompleteness and inclusion of false matches will somewhat offset in the effects on the normalization

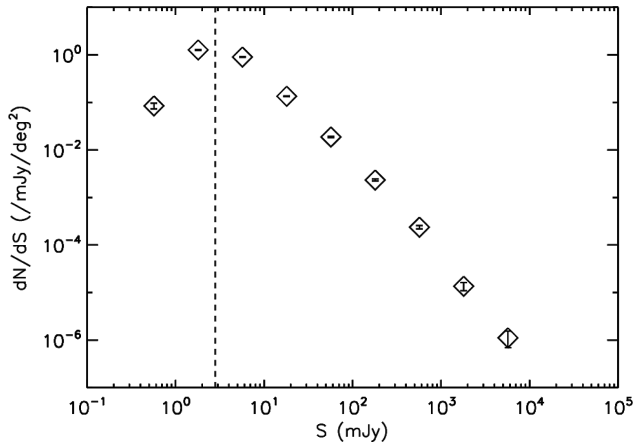


Figure 1. Number of objects per interval of 1.4 GHz flux density in the parent sample (diamonds). The vertical dashed line shows the flux density limit ($S_{1.4\text{GHz}} > 2.8$ mJy) applied in this paper. The number counts are still rising at this flux density.

of the luminosity functions. We do not do any scaling of the luminosity functions to account for input catalogue incompleteness but note that its effect on the normalization could not be more than a few per cent.

A possible systematic could arise if the incompleteness or false matches are biased towards a particular source type or source properties. The most likely source of such a bias is the behaviour of the matching algorithm for sources with complex (non-point source) radio morphologies. Such sources are more common at low redshift and lower luminosity as a result of angular resolution effects and the presence of extended star-forming galaxies. There is no evidence for such a bias. Only ~ 10 per cent of the sample is matched to more than one FIRST component, which is consistent with other determinations from the literature (Ivezić et al. 2002). Of those ~ 10 per cent the fraction of matches to the random catalogues are almost identical for FIRST sources with two, three and four or more components.

While the high spatial resolution of the FIRST catalogue makes it preferable for matching to the optical photometry it will also resolve out extended radio emission resulting in lower flux density measurements. Since angular size decreases with redshift this flux loss will be more significant at low redshift and could mimic evolution in the radio luminosity function. To avoid this, we replace the flux densities with those measured from the lower spatial resolution NRAO VLA Sky Survey (NVSS; Condon et al. 1998) catalogue. In the case where a single NVSS source coincides with more than one FIRST source the NVSS flux is split between objects with the same flux ratio as measured by FIRST (see Ching 2015 for details of the matching of FIRST and NVSS sources).

At the faintest flux densities the NVSS catalogue will suffer from significant incompleteness. To avoid working with a parent sample that suffers from such incompleteness, we only include objects with flux density greater than 2.8 mJy in constructing our luminosity function. This is the same flux limit adopted by Sadler et al. (2007) when matching radio sources to the luminous red galaxies in the 2dF-SDSS LRG and QSO survey (2SLAQ; Croom et al. 2009). With this flux-density limit the source counts are still rising at the faintest flux densities; as demonstrated in Fig. 1. This results in a sample of 10 827 matched radio/optical sources.

The optical spectroscopy for the sample was gathered either from publicly available archival sources such as the SDSS (Adelman-

McCarthy et al. 2008), 2SLAQ (Cannon et al. 2006; Croom et al. 2009) and the 2dF QSO redshift survey (2QZ; Croom et al. 2004) or from a dedicated ‘spare-fibre’ campaign using the 2dF/AAOmega instrument on the Anglo-Australian Telescope. This was done by ‘piggy-backing’ on the WiggleZ Dark Energy Survey (WiggleZ; Drinkwater et al. 2010) and GAMA (Baldry et al. 2010; Driver et al. 2011; Liske et al. 2015) large survey programmes by using a small number of fibres on each survey field to target radio galaxies (see Ching (2015) for details). This has almost no impact on the large survey efficiency but over time results in a large number of ‘spare-fibre’ spectra being obtained. Of the 10 827 radio galaxies satisfying our 1.4 GHz flux density criterion, the number with optical spectra is 7088. Of these 6215 are deemed to have reliable redshift determinations (~ 87 per cent).

2.1 Optical spectroscopic classification

In addition to providing an accurate measure of the redshift the optical spectroscopy can be used to determine the physical origin of the radio emission, i.e. star formation or AGN. The optical spectroscopy can also be used to separate the AGN into LERGs and HERGs. Full details of the semi-automatic classification procedure is given in Ching (2015). In brief, FIRST galaxies whose radio emission is dominated by star formation are identified using a Baldwin, Phillips and Terlevich (hereafter BPT; Baldwin, Phillips & Terlevich 1981) diagram. Only galaxies with radio luminosity $L_{1.4\text{GHz}} \leq 10^{24}$ W Hz⁻¹ and $z < 0.3$ are considered, since galaxies more powerful than this would require unrealistically high star formation rates and so are assumed to have their radio emission generated by an AGN. The BPT diagnostic will not work in the case where the galaxy has a radio-quiet optical AGN and radio emission powered by star formation (Best & Heckman 2012; Ching 2015). These cases were identified based on a comparison of the inferred star formation rates from H α and radio luminosity. The remaining radio galaxies are classified as AGN and further subdivided using the equivalent width of the [O III] λ 5007 emission line, where galaxies are classified as HERGs if they have $\text{SNR}([\text{O III}]\lambda 5007) > 3$ and $\text{EW}([\text{O III}]\lambda 5007) > 5$ Å. See Ching (2015) for a detailed description of the methods used to make the line strength measurements. The 5 Å demarcation is the same as that used by Best & Heckman (2012).

The O [III] λ 5007 line is redshifted out of the WiggleZ and SDSS spectra at $z \sim 0.83$ and out of the GAMA spectra at $z \sim 0.76$. These also correspond, approximately, to the redshift where our optical k -corrections are expected to be reliable (Blanton & Roweis 2007). In addition, as a result of the magnitude limit of the optical spectroscopic follow-up, above $z \sim 0.75$ the spectroscopic sample is dominated by broad-line AGN and there are almost no narrow-line AGN or LERGs in the sample (see Fig. 2). We therefore impose a redshift limit of $z = 0.75$ for construction of our luminosity functions. We also apply a lower redshift limit of $z = 0.005$ to remove Galactic objects. With these cuts the final number of objects, with reliable redshifts, is 5026. A summary of the number of spectra from each survey in these final 5026 objects is given in Table 1. Not all objects can be classified using the semi-automated methods of Ching (2015). Out of the 5026 objects in our sample, 284 (~ 6.7 per cent) were not classified by Ching (2015). A fraction of the spectra in the Ching (2015) sample had been inspected and classified visually, and in the cases where there is no automated classification but a visual one, we use this visual classification. This leaves 229 objects (corresponding to ~ 4.6 per cent) without a classification. Rather than carry these unclassified objects through

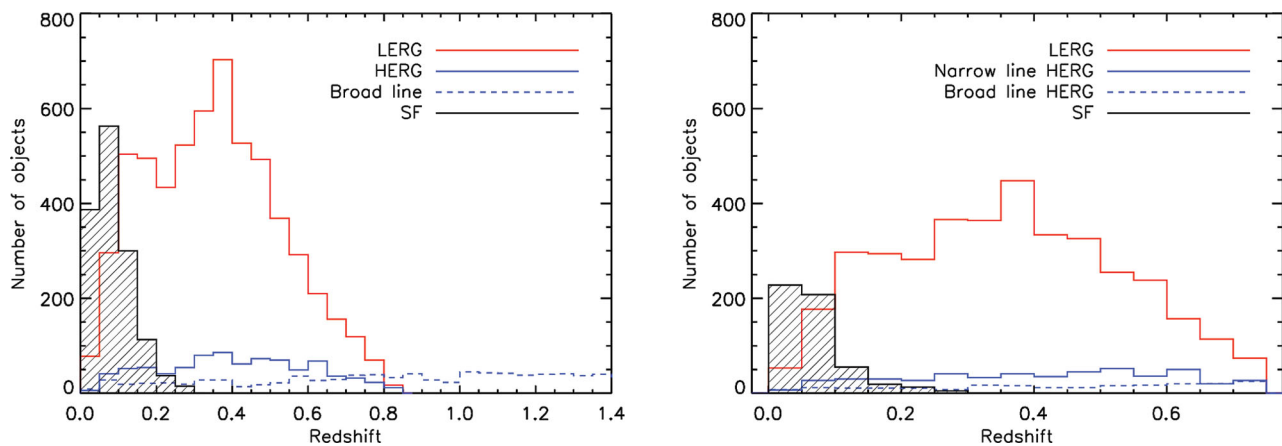


Figure 2. Left-hand panel: the redshift distribution of all radio galaxies with reliable spectroscopic redshifts. The redshift distributions for star-forming galaxies, LERGs and HERGs are shown separately. Above $z \sim 0.8$, the sample is dominated by broad-line AGN. Right-hand panel: the $n(z)$ of the sample used to construct luminosity functions in this paper after selecting objects with $0.005 < z < 0.75$ and $S_{1.4\text{GHz}} > 2.8$ mJy.

Table 1. A summary of the number of spectra from each survey in these final 5026 objects which are used in the measurement of the luminosity functions.

	$z < 0.3$	$0.3 \leq z < 0.5$	$0.5 \leq z < 0.75$	Total
$N(\text{SDSS})$	1958	846	221	3025
$N(\text{WiggleZ main})^a$	26	137	151	314
$N(\text{WiggleZ radio})^b$	72	354	389	815
$N(\text{WiggleZ other})^c$	9	15	40	64
$N(\text{GAMA})$	154	298	221	673
$N(\text{2SLAQ LRGs})$	0	32	95	127
$N(\text{2SLAQ QSOs})$	1	1	3	5
$N(\text{2QZ/6QZ})$	1	1	1	3
Total	2221	1684	1121	5026

Notes. ^aWiggleZ main survey targets.

^bSpare fibre targets for this project.

^cTarget for other spare fibre programs.

the analysis we performed visual classification of these sources. For the most part this was straightforward. The fraction of objects classified as each type visually are similar to the overall fractions but with a lower frequency of ‘star-forming’ objects and a higher fraction of HERGs. The fractions of objects of each type prior to the visual classification are ~ 75.2 , 14.3 and 10.5 per cent for the LERGs, HERGs and star-forming galaxies, respectively. The corresponding fractions in the visual classification are ~ 78.6 , 20.9 and 0.5 per cent. The increase in the HERG fraction (including quasars) and the decrease in the star-forming fraction is expected since the redshift distribution of the unclassified objects is, not surprisingly, peaked at the high-redshift end of the sample.

3 THE RADIO LUMINOSITY FUNCTION

We first wish to construct the bivariate luminosity function for all galaxies in the optical-radio matched sample in multiple redshift bins. That is, we calculate the volume density of galaxies per interval of radio luminosity per interval of optical luminosity in each redshift bin. To do this we use the standard $1/V_{\text{max}}$ method (Schmidt 1968), where the number density in each bin is given by

$$\Phi(M_i, L_{1.4\text{GHz}}) \Delta M_i \Delta \log L_{1.4\text{GHz}} = \sum_{\text{gal}} \frac{w_{\text{gal}}}{V_{\text{max}}(\text{gal})}. \quad (1)$$

The sum on the right-hand side is over all galaxies in the bin. The weight, w_{gal} , given to each galaxy corrects for incompleteness in the spectroscopic follow-up. For a complete survey $w_{\text{gal}} = 1$ and for incomplete samples w_{gal} is given by the reciprocal of the completeness. The denominator, $V_{\text{max}}(\text{gal})$, is the maximum volume over which the galaxy could have been observed given the selection limits in both the radio and optical. We outline our methods for estimating w_{gal} and $V_{\text{max}}(\text{gal})$ below.

3.1 Estimating the completeness

The overall spectroscopic completeness is given by the number of targets for which we obtained a spectrum of sufficient quality to make a reliable redshift measurement divided by the number of targets in the parent radio/optical matched sample. That is $6215/10\,827$ or ~ 57 per cent. This is mostly targeting incompleteness; the percentage of spectroscopically targeted objects which resulted in a good quality redshift classification, i.e. spectroscopic completeness, is ~ 90 per cent. This spectroscopic incompleteness is not random. It will depend sensitively on the optical magnitude for at least two reasons. First, the optical spectroscopy of the sample is constructed from spectroscopy from multiple surveys, which have different limiting magnitudes. In addition, the spectroscopic completeness within an individual survey generally decreases with optical magnitude as the noisier spectra obtained for fainter galaxies make it increasingly difficult to identify the redshift. Ching (2015) used repeat observations to demonstrate that there is little difference in the likelihood of obtaining a redshift for different spectral classes (with and without emission lines) once optical magnitude is taken into account. They did this by comparing the fraction of objects of different spectral classes that required more than one repeat observation to acquire a good redshift. The idea being that if for a particular source type it is easier to identify a redshift (at give apparent magnitude) than it should, on average, require less repeat observations. While they did find a slightly higher tendency for spectra without emission lines to require a repeat observation than those with emission lines, it was not statistically significant. One important caveat on this technique is that it can only be used in cases where a reliable redshift is eventually obtained by one of the observations.

The completeness will also be sensitive to colour, again for at least two distinct reasons. First, while most of spectra were obtained

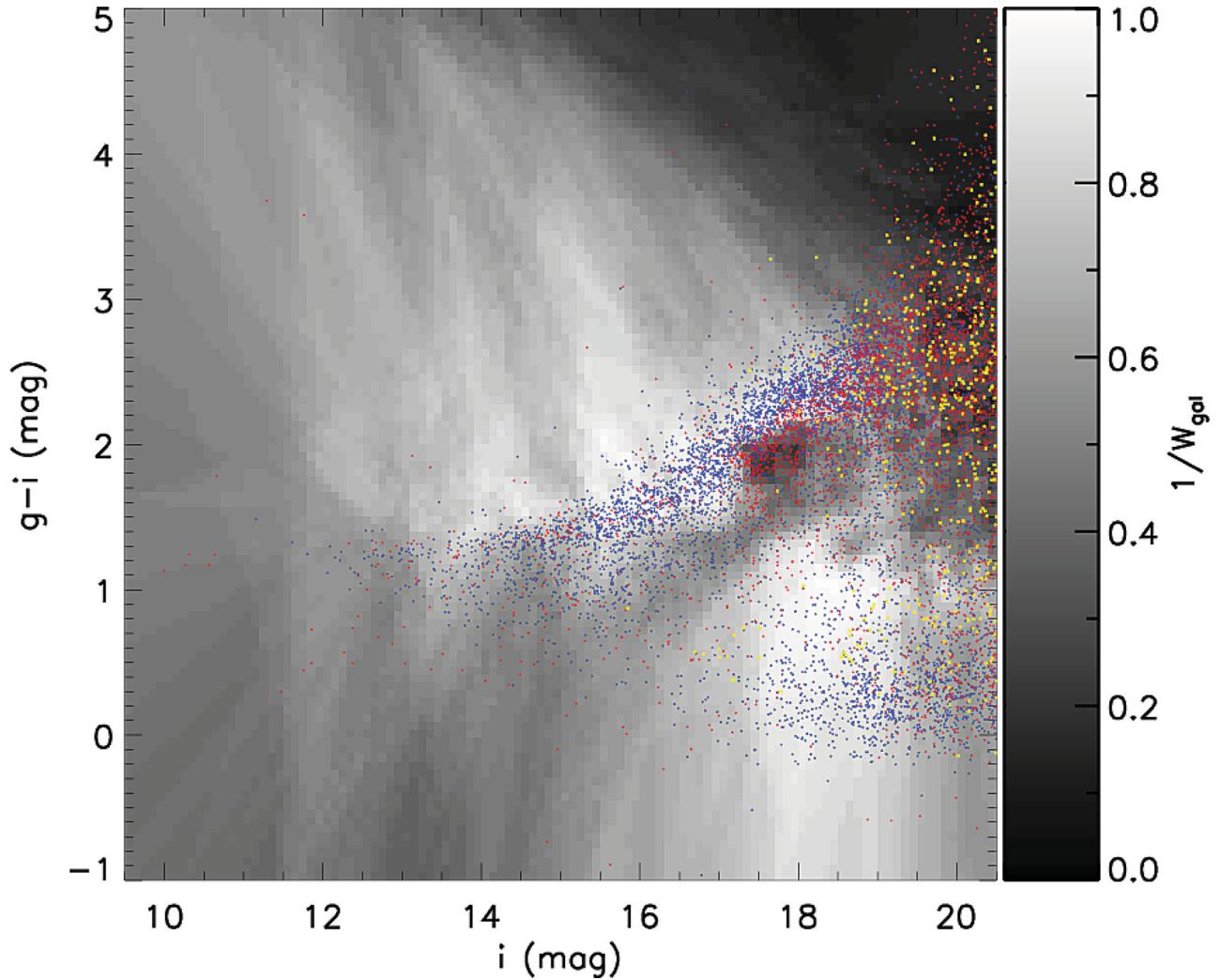


Figure 3. The completeness map in the i -magnitude versus $g - i$ colour plane, used to generate the weight (w_{gal} ; shown in side bar) assigned to each galaxy in constructing the luminosity function. Overlaid blue points are the photometric sample objects above our 2.8 mJy flux limit for which a reliable redshift has been obtained. The overlaid red points are objects for which no spectroscopic follow-up observation was made. The yellow points represent objects which were observed spectroscopically but a reliable redshift could not be determined. The structure in the completeness map, such as the low completeness for faint objects with $g - i$ colours of ~ 1 – 2 mag, is mostly the result of targeting completeness in the constituent surveys and demonstrates the importance of constructing our completeness estimates in this plane.

from surveys that do not apply colour selection criteria (e.g. our dedicated follow-up, targets with SDSS spectra and the GAMA main survey), a fraction of the spectra come from surveys that do (e.g. the WiggleZ main survey, 2SLAQ and 2QZ). Another reason completeness will vary with colour, is that colour correlates with other spectral properties which make a redshift easier to identify. In particular, galaxies with bluer colour are more likely to have easy to identify emission lines. Although, as mentioned above, this appears to cause little bias.

There may be other properties which influence the spectroscopic completeness (e.g. changes in the observable spectral features in a fixed observing band with redshift) but it is likely that magnitude and colour account for the dominant dependences. We therefore choose to construct our spectroscopic completeness in this plane, specifically we calculate our completeness (and hence our w_{gal} 's) in the i -magnitude versus $g - i$ plane.

We calculate the completeness for each object (or position) in the i -magnitude versus $g - i$ plane by averaging over an adaptively

sized circle in this plane. The size of the circle is calculated by using the distance in the plane to the 50th nearest neighbour in the photometric input catalogue. Using this adaptive bin size for estimating the completeness means in regions of the plane with few objects we still use a reasonable number of objects in estimating the completeness, while in high-density regions we obtain a finer more local sampling of the completeness. The completeness in this plane is shown in Fig. 3. Each galaxy is assigned a w_{gal} given by the reciprocal of the completeness. Using this nearest neighbour method for estimating the completeness even objects with large weights have had their completeness estimated using a reasonable number of objects. For example, for an object with a weight of 10 (completeness of 0.1) the estimate is based on five objects with good spectra and 50 objects in the input catalogue. We also checked that our luminosity functions are not largely affected by objects with the highest weights. Removing objects with weights greater than 10 makes no significant quantitative difference and no qualitative difference to our results.

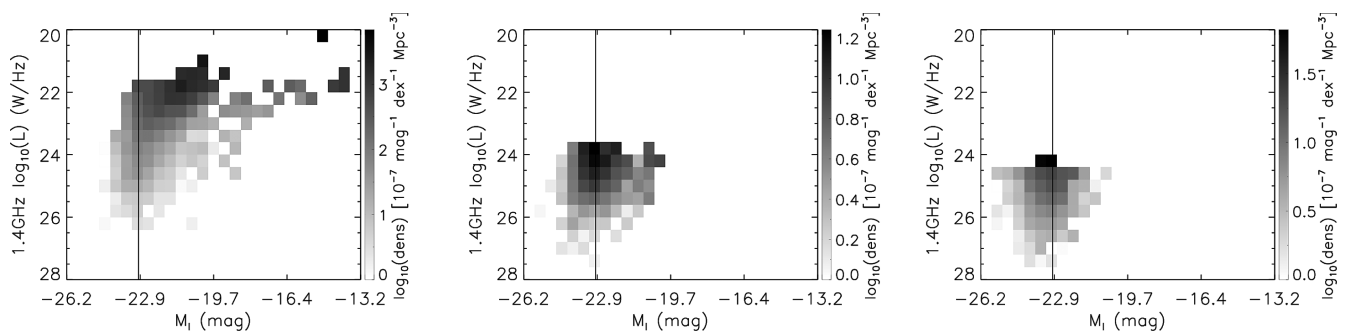


Figure 4. The bivariate luminosity distribution. The space density represented by a colour-scale in the optical magnitude–radio luminosity plane. The panels are for the different redshift bins: left: $0.005 < z < 0.30$; middle: $0.30 < z < 0.50$; and right: $0.5 < z < 0.75$. The flux-density and apparent magnitude selection limits correspond to progressively brighter radio and optical luminosity limits with increasing redshift. The absolute magnitude limit applied when analysing the redshift evolution of the radio luminosity function is shown as the vertical line. This corresponds to the absolute magnitude limit at the high-redshift edge of the highest redshift bin not inclusive of an e -correction.

3.2 Estimating V_{\max}

To evaluate equation (1), and correctly weight the contribution to the luminosity function of each galaxy in our sample, we need to estimate the volume within which each galaxy would satisfy the optical and 1.4 GHz flux density selection limits, i.e. V_{\max} . This volume will depend on the redshift of the source, its optical magnitude, 1.4 GHz flux density, and the spectral shape in both the optical and radio regimes. To do this, for each source, we first calculate the absolute i -band magnitude including a k -correction and evolutionary correction:

$$M_i = m_i - DM - K_i(z) - e(z), \quad (2)$$

where DM is the distance modulus, $K_i(z)$ is the k -correction and $e(z)$ is the evolutionary correction (e -correction). The k -correction is calculated using version v4_2 of the `KCORRECT` package (Blanton & Roweis 2007) using the five band (u, g, r, i, z) SDSS photometry. The e -correction accounts for the fading of stellar populations with time. For the LERGs we use the e -corrections for early-type galaxies from Poggianti (1997). The HERGs are generally bluer, more likely to be interacting and star-forming (or recently star-forming) systems which mitigates the effect on the overall optical luminosity of the ageing of the underlying older stellar population. Given this we set $e(z) = 0$ for the HERGs and discuss the effects this assumption has on the evolution of the luminosity function in Section 4. It is worth noting that the magnitude of the e -correction is significant: increasing from ~ 0.1 mag (i -band) at $z = 0.1$ to ~ 0.8 mag at $z = 0.75$.

We then calculate the radio luminosity, also including a k -correction:

$$L_{1.4\text{GHz}} = 4\pi d_L^2 \frac{1}{(1+z)^{(1+\alpha)}} S_{1.4\text{GHz}} \quad (3)$$

here d_L is the luminosity distance and α is the spectral index, defined as $S_\nu = \nu^\alpha$. We assume the canonical $\alpha = -0.7$ (Condon, Cotton & Broderick 2002; Sadler et al. 2002). Within reasonable spectral index limits this assumption has no significant effect on the derived luminosity functions.

We then evaluate S_ν and m_i using equations (2) and (3) at a series of redshifts ($\Delta z = 0.005$) and find the minimum and maximum redshifts where the source satisfies both the optical and radio selection criteria as well as the limits of the redshift range being analysed (i.e. the appropriate redshift bin boundaries). We can then calculate the integrated comoving volume over which the source could have been observed, i.e. V_{\max} .

3.3 The bivariate luminosity function

In Fig. 4 we have plotted the bivariate luminosity function for all radio galaxies (including HERGs, LERGs and star forming) constructed using equation (1) in three redshift bins. The left-hand panel is the luminosity function from our ‘local’ redshift bin: $0.005 < z < 0.3$. It can be seen that the number density of radio galaxies rises steeply with decreasing radio luminosity. There is a significant contribution to the radio galaxy density from objects at faint optical magnitudes and low radio luminosities. There is a large variance between the bivariate luminosity function bins for these objects. Much of this contribution comes from local radio galaxies where the radio emission arises from star formation rather than from an AGN (see right-hand column of Fig. 6). The noise is due to the small volume (and hence absolute numbers) in which these object satisfy the selection limits.

The middle and right-hand panels show the bivariate luminosity function for redshift bins $0.3 < z < 0.5$ and $0.5 < z < 0.75$, respectively. As a consequence of the flux density limits in both the optical and radio, the luminosity function is restricted to progressively brighter (in both optical luminosity and radio luminosity) galaxies in the higher redshift bins. In all redshift bins the space density increases with decreasing radio luminosity.

Later, when we consider redshift evolution in the radio luminosity function we will restrict our analysis to a subset of galaxies with $M_i < -23$ (corresponding to the faintest galaxies we can detect at $z = 0.75$). This limit is overplotted as a vertical black line on Fig. 4.

3.4 The local radio luminosity function

In order to produce a radio luminosity function, we marginalize the bivariate luminosity function over optical luminosity. That is, we calculate the space density of radio galaxies, per radio luminosity bin, integrated over all observed optical luminosities. In Fig. 5, we produce the local radio galaxy luminosity function. The radio luminosity function for all radio galaxies is plotted as *open diamonds* and the luminosity functions separated for AGN and star-forming galaxies are plotted as *open triangles* and *open squares*, respectively. Below a radio luminosity of $\sim L_{1.4\text{GHz}} \sim 10^{23} \text{ W Hz}^{-1}$ the star-forming galaxies dominate the space density of sources, while above this luminosity the AGN population dominates. These luminosity functions are also tabulated in Table 2.

Also in Fig. 5, we overplot as *blue lines* the local radio luminosity function of 6dFGRS galaxies from Mauch & Sadler (2007) for all radio galaxies (*solid line*), AGN (*dot-dashed line*) and

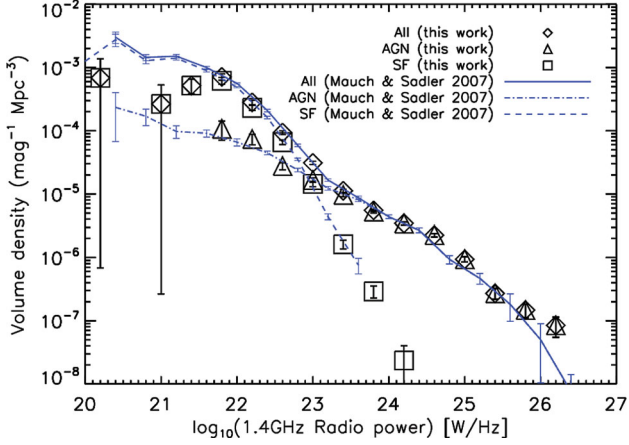


Figure 5. The radio luminosity function for our $0.005 < z < 0.3$ redshift bin (diamonds). Also, plotted the luminosity function separated into radio AGN (triangles) and star-forming radio galaxies (squares). The star-forming galaxies outnumber the AGN below $P_{1.4\text{GHz}} \sim 10^{23} \text{ W Hz}^{-1}$ but contribute very little to the number density at higher radio luminosities. Also shown is the radio luminosity functions from Mauch & Sadler (2007) for all sources (solid blue line), radio AGN (dot-dashed blue line) and radio star-forming galaxies (dashed blue line).

star-forming galaxies (*dashed line*). Our luminosity functions and those of Mauch & Sadler (2007) are in good agreement and the local radio luminosity function of Mauch & Sadler (2007) is known to be in good agreement with determinations measured by other authors (Machalski & Godlowski 2000; Sadler et al. 2002; Best & Heckman 2012; Mao et al. 2012). It should be noted that the comparison of these luminosity functions is not expected to be exact. It is clear from the bivariate luminosity functions in Fig. 4 that the space density of radio galaxies measured will depend on the range of optical luminosities sampled. The fainter our optical limits the more galaxies at a given radio luminosity we will find. Strictly then, to compare radio luminosity functions we should integrate over the same optical magnitude range to ensure consistency. For local luminosity functions this effect should be small, since at the lowest

redshifts all surveys will probe down to very faint optical magnitudes (albeit noisily because of the reducing volume) and the $1/V_{\text{max}}$ correction will return approximately the same luminosity function. However, when comparing luminosity functions at different redshifts it is important to use the same range of optical luminosities, as demonstrated in Figs 4 and 6.

3.5 Separating the luminosity function of radio AGN by accretion mode

As described in Section 2.1 the AGN in our sample have been classified as either LERGs or HERGs based on their optical spectral properties. In Fig. 6 we show the bivariate luminosity function for LERGs (left-hand column), HERGs (middle column) and star-forming radio galaxies (right-hand column) in three redshift bins (top to bottom). The star-forming radio galaxies are shown only for the low redshift bin, since there are no such objects in the catalogue with higher redshifts.

In Fig. 7 (and tabulated in Table 2), we show the radio luminosity functions for LERGs and HERGs separately, for AGN in our ‘local’ $0.005 < z < 0.3$ redshift bin. We have summed over optical luminosities down to the limit of our sample ($m_i < 20.5$). The local LERG and HERG luminosity functions of Best & Heckman (2012, parameters taken from Heckman & Best 2014) are also shown (*solid lines*). The LERG luminosity functions are similar in shape and normalization. The HERG luminosity functions, however, are significantly different. The HERG luminosity function presented here has a higher space density, especially at low radio luminosities. As noted earlier, we do not expect radio luminosity functions to agree unless they sample the same range of optical luminosities, however, when measured locally this effect should be small and cannot explain the discrepancy.

In the case of the HERGs there are also differences in the classification techniques. Best & Heckman (2012) were deliberately strict in removing star-forming radio galaxies. This conservative approach is well justified since at the faint end of the radio luminosity function the star-forming radio galaxies can dominate in number density over the AGN by approximately an order of magnitude (see

Table 2. The local ($0.005 < z < 0.3$) 1.4 GHz radio luminosity function from this sample separated into radio AGN and star-forming galaxies. The radio AGN are further separated into LERGs and HERGs.

$\log_{10} P_{1.4}$ (W Hz ⁻¹)	<i>N</i>	All galaxies log(Φ) (mag ⁻¹ Mpc ⁻³)	<i>N</i>	SF galaxies log(ϕ) (mag ⁻¹ Mpc ⁻³)	<i>N</i>	Radio AGN log(Φ) (mag ⁻¹ Mpc ⁻³)	<i>N</i>	LERGs log(Φ) (mag ⁻¹ Mpc ⁻³)	<i>N</i>	HERGs log(Φ) (mag ⁻¹ Mpc ⁻³)
21.00	1	$-3.58^{+0.30}_{-3.00}$	1	$-3.58^{+0.30}_{-3.00}$						
21.40	14	$-3.28^{+0.10}_{-0.13}$	14	$-3.28^{+0.10}_{-0.13}$						
21.80	76	$-3.15^{+0.05}_{-0.05}$	67	$-3.21^{+0.05}_{-0.06}$	9	$3.97^{+0.12}_{-0.18}$	8	$-4.00^{+0.13}_{-0.19}$	1	$-4.75^{+0.30}_{-3.00}$
22.20	156	$-3.55^{+0.03}_{-0.04}$	128	$-3.64^{+0.04}_{-0.04}$	28	$-4.13^{+0.08}_{-0.09}$	22	$-4.19^{+0.08}_{-0.10}$	6	$-5.06^{+0.15}_{-0.23}$
22.60	208	$-4.03^{+0.03}_{-0.03}$	144	$-4.18^{+0.03}_{-0.03}$	64	$-4.56^{+0.05}_{-0.06}$	46	$-4.72^{+0.06}_{-0.07}$	18	$-5.07^{+0.09}_{-0.12}$
23.0	255	$-4.51^{+0.03}_{-0.03}$	109	$-4.84^{+0.04}_{-0.04}$	146	$-4.78^{+0.03}_{-0.04}$	124	$-4.85^{+0.04}_{-0.04}$	22	$-5.58^{+0.08}_{-0.10}$
23.40	314	$-4.95^{+0.02}_{-0.03}$	41	$-5.79^{+0.06}_{-0.07}$	273	$-5.09^{+0.03}_{-0.03}$	234	$-5.09^{+0.03}_{-0.03}$	39	$-5.84^{+0.06}_{-0.08}$
23.80	440	$-5.26^{+0.02}_{-0.02}$	21	$-6.54^{+0.09}_{-0.11}$	419	$-5.28^{+0.02}_{-0.02}$	368	$-5.34^{+0.02}_{-0.02}$	51	$-6.15^{+0.06}_{-0.07}$
24.20	349	$-5.46^{+0.02}_{-0.02}$	2	$-7.63^{+0.23}_{-0.53}$	347	$-5.47^{+0.02}_{-0.02}$	319	$-5.52^{+0.02}_{-0.02}$	28	$-6.43^{+0.08}_{-0.09}$
24.60	242	$-5.65^{+0.03}_{-0.03}$			242	$-5.65^{+0.03}_{-0.03}$	217	$-5.71^{+0.03}_{-0.03}$	25	$-6.52^{+0.08}_{-0.10}$
25.00	112	$-6.03^{+0.04}_{-0.04}$			112	$-6.03^{+0.04}_{-0.04}$	101	$-6.07^{+0.04}_{-0.05}$	11	$-7.04^{+0.11}_{-0.16}$
25.40	27	$-6.57^{+0.08}_{-0.09}$			27	$-6.57^{+0.08}_{-0.09}$	20	$-6.78^{+0.09}_{-0.11}$	7	$-6.98^{+0.14}_{-0.21}$
25.80	17	$-6.83^{+0.09}_{-0.12}$			17	$-6.83^{+0.09}_{-0.12}$	7	$-7.26^{+0.14}_{-0.21}$	10	$-7.03^{+0.12}_{-0.16}$
26.20	8	$-7.07^{+0.13}_{-0.19}$			8	$-7.07^{+0.13}_{-0.19}$	3	$-7.42^{+0.20}_{-0.37}$	5	$-7.33^{+0.16}_{-0.26}$

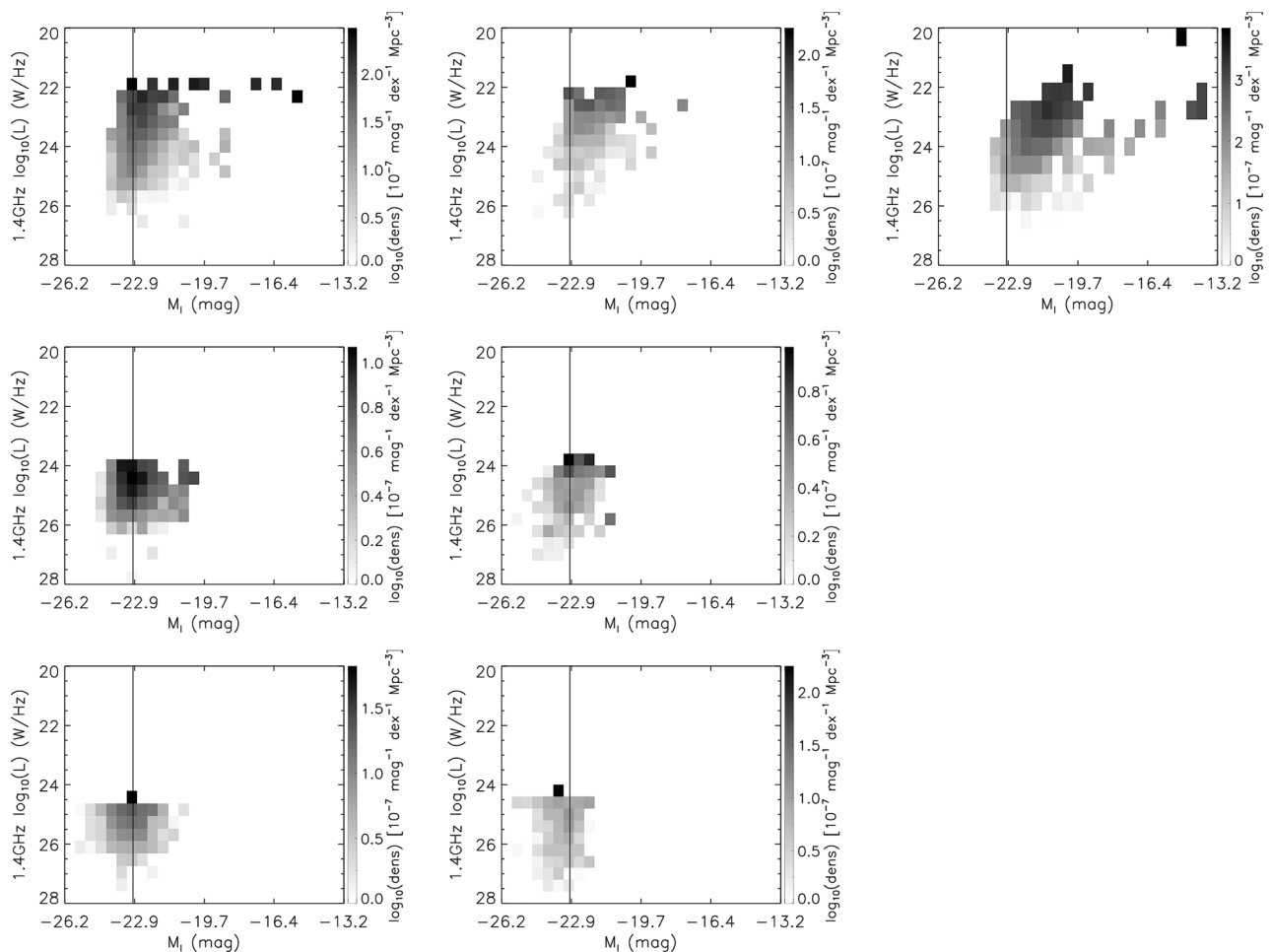


Figure 6. The bivariate luminosity distribution for LERGs (left-hand column), HERGs (middle column) and star-forming radio galaxies (right-hand column). The rows are for the different redshift bins: top row: $0.005 < z < 0.30$; middle row: $0.30 < z < 0.50$; and bottom row: $0.5 < z < 0.75$. Only the lowest redshift bin is shown for the star-forming radio galaxies since there are no objects with this classification in higher redshift bins. The flux-density and apparent magnitude selection limits correspond to progressively brighter radio and optical luminosity limits with increasing redshift. The absolute magnitude limit applied when analysing the redshift evolution of the radio luminosity function is shown as the vertical line. This corresponds to the absolute magnitude limit at the high-redshift edge of the highest redshift bin.

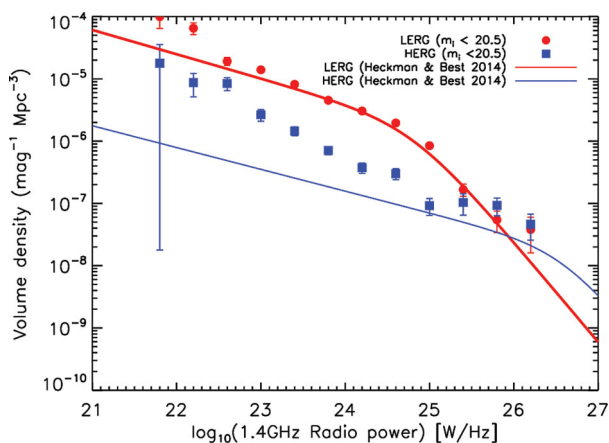


Figure 7. The radio luminosity function of AGN in our $0.005 < z < 0.3$ redshift bin separated into LERGs (red filled circles) and HERGs (blue filled squares) summed over optical magnitudes down to our limit of $i < 20.5$. Overplotted are the luminosity functions of local LERGs (red solid line) and HERGs (blue solid line) from Heckman & Best (2014).

Fig. 5). In this case misclassifying a small fraction of star-forming galaxies as AGN can have a considerable effect on the measured space density of AGN.

Based on comparison of common objects, some radio galaxies classified as star-forming radio galaxies by Best & Heckman (2012) are expected to be classified as HERGs in this sample (Ching 2015). Best & Heckman (2012) use a combination of three tests to remove radio galaxies where the radio emission is suspected to arise from star formation: a standard BPT emission line diagnostic; a ratio of radio-to-emission-line luminosity; and a method using the strength of the 4000 Å break (measured via the D4000 index) and the ratio of radio luminosity to stellar mass. While Ching (2015) used methods similar to the first two – they do not apply the third. The reason for this is twofold. First, some of the spectra (such as those derived from the WiggleZ survey) have low continuum signal to noise and poor correction of the wavelength response – meaning the 4000 Å break strength cannot be accurately measured. Secondly, while Best & Heckman (2012) include objects classified as QSOs, they only do so if they were targeted as galaxies (i.e. not point-sources). In contrast, the catalogue of Ching (2015) includes broad-line and point-like

objects. A test involving the D4000 strength is inappropriate for such objects since they will have strong blue continuum.

In addition, while a D4000 test is well justified for the LERGs which are a well-separated population having strong D4000 strengths well above the star-forming cut – this is not true for the narrow-line HERGs. Radio galaxies classified as HERGs using a BPT diagnostic have a significant fraction of the population within the star-forming region. These are likely HERGs incorrectly classified as star-forming galaxies using this criterion (see *left middle panel* of fig. 9 in Best et al. 2005). As another example, Herbert et al. (2010) measure the D4000 strength for a population of high-power HERGs where the radio emission clearly arises from AGN activity. This population has an approximately uniform distribution of D4000 strengths between ~ 1.1 and 1.7 . While most of these galaxies would be classified as AGN because of their high radio power, since the stellar population will fade on time-scales much longer than the time-scale on which radio activity can change such objects can move into an area of parameter space where they would be misclassified as HERGs. While many of the radio AGN misclassified as star-forming using this test can be correctly classified based on the other two test (see Best & Heckman 2012, appendix A2) these examples again demonstrate the difficulty in separating HERGs and star-forming radio galaxies.

In Fig. 8, we demonstrate that the differences between our local HERG luminosity function and that of Best & Heckman (2012) can be explained by differences in the classifications in the star-forming objects (at low radio powers) and the inclusion of broad-line objects (at $L_{1.4\text{GHz}} \sim 10^{24} \text{ W Hz}^{-1}$). In the top panel of Fig. 8, we show the local luminosity function of the star-forming radio galaxies (dotted lines) and HERGs (dashed lines) for our sample (blue) and that of Best & Heckman (2012, red). The solid lines show the sum of the HERGs and star-forming luminosity functions. The luminosity functions of the sum are well matched at the faint end between the two samples. The difference being some objects classified as HERGs by Ching (2015) were removed as star-forming galaxies by Best & Heckman (2012).

There is, however, a difference at $L_{1.4\text{GHz}} \sim 10^{24} \text{ W Hz}^{-1}$ with the number density of objects in our sample being higher by a factor of ~ 2 . In the bottom panel, we show the same luminosity functions but with the broad-line objects removed from our HERG luminosity function. The two determinations are in much better agreement and the remaining difference is not statistically significant.

The determination of the true HERG luminosity function at low radio power is a fundamentally difficult problem stemming from the fact that the number density of star-forming radio galaxies is so high in this regime. A faultless classification would likely require high spatial resolution radio continuum imaging. However, it is not critical in the context of this paper, i.e. measuring the redshift evolution of the luminosity function. This is because the radio luminosity limits in our higher redshift bins (set by our flux limit) are outside the regime where star formation powered radio galaxies are important. For example, even in our intermediate redshift bin we are restricted to radio luminosities $L_{1.4\text{GHz}} \gtrsim 10^{24} \text{ W Hz}^{-1}$. Above these radio luminosities the number density of HERGs quickly rises above the star-forming galaxies, regardless of the classification method used.

3.6 Fitting radio luminosity functions

Several analytical forms have been proposed as good representations of galaxy luminosity functions. The radio luminosity function is often fitted with a double power law (e.g. Dunlop & Peacock

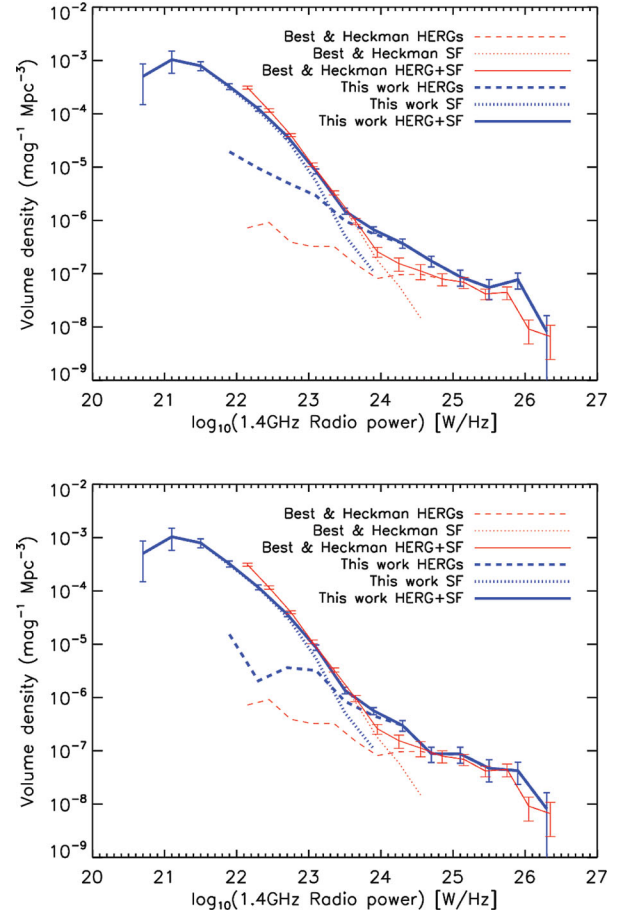


Figure 8. Top panel: the radio luminosity function of star-forming radio galaxies (blue dotted line), HERGs (blue dashed line) and their sum (blue solid line) in our sample and those from Best & Heckman (2012, red dotted, red dashed and red solid lines, respectively). The bottom panel is the same as the top panel but with the broad-line AGN removed from our HERG sample.

1990; Brown, Webster & Boyle 2001; Mauch & Sadler 2007) of the form

$$\Phi(L) = \frac{\Phi^*}{(L^*/L)^\alpha + (L/L^*)^\beta}. \quad (4)$$

Saunders et al. (1990) proposed a function which behaves as a power law at low radio luminosity and lognormal at high radio luminosities:

$$\Phi(L) = \Phi^*(L/L^*)^{1-\alpha} \exp\left(-\frac{1}{2\sigma^2}(\log^2(1 + L/L^*))\right) \quad (5)$$

which has been commonly used to parametrize the radio galaxy luminosity function (e.g. Saunders et al. 1990; Sadler et al. 2002; Smolčić et al. 2009). Optical galaxy luminosity functions are usually represented by a power law with an exponential cut-off at the bright end:

$$\Phi(L) = \Phi^*(L/L^*)^\alpha \exp(-L/L^*), \quad (6)$$

i.e. the Schechter function (Schechter 1976). This function has the advantage of having one less parameter than the other two. We tested each of these functional forms in fitting the radio luminosity functions in this paper, including fitting for redshift evolution.

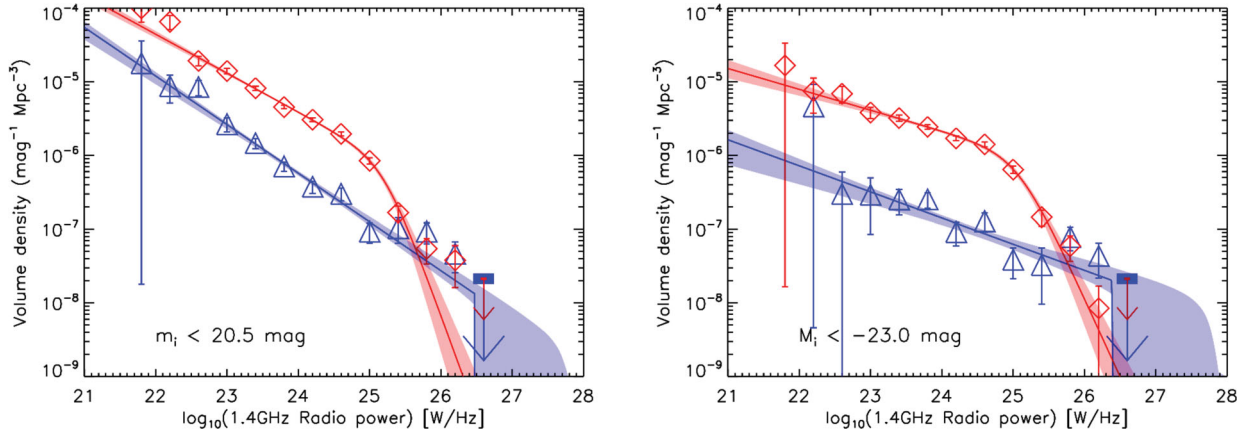


Figure 9. The radio luminosity function of AGN in our $0.005 < z < 0.3$ redshift bin separated into LERGs (red diamonds and solid line) and HERGs (blue triangles and solid line). Left-hand panel: integrated over $i < 20.5$ and right-hand panel: galaxies with $M_i < -23$ only. Overplotted are double power-law fits to the data (solid lines).

In the case of the HERGs all three functional forms perform comparably with, for example, the difference in Akaike Information Criterion (AIC; Akaike 1974) in every case being less than 3. An issue which arises in fitting the HERG population is the small number of objects at the bright end where the number density decreases rapidly. In the case of the double power-law fit (equation 4) this manifests itself as a poor constraint on the bright-end slope β . The sharp drop off in density at high radio luminosities and poor statistics means that a good fit can be obtained for arbitrarily large negative β (i.e. as $\beta \rightarrow -\infty$ the power-law slope becomes vertical). Similarly, for the fitting function of equation (5) the σ parameter is poorly constrained. The Schechter function fits the data well at the bright end, although it is not significantly preferred to the other models overall.

For the LERGs both equations (4) and (5) allow good analytical representations of the data, with little difference in the maximum likelihoods. On the other hand, the Schechter (1976) function is entirely inappropriate ($\Delta\text{AIC} \gtrsim 20$ in comparison to the other models when fitting for redshift evolution). For our purposes, the most important check is that measuring the rate of redshift evolution (i.e. the K_L and K_D parameters in equations 7 and 9) is robust. This is true, since the change in the best-fitting value of these parameters between the models is small in comparison to their uncertainties.

In this paper, we have chosen to use the double power-law representation of equation (4) when fitting the radio luminosity functions. Because of the poor constraints at the bright end of the HERGs, we use a logarithmic prior on the β parameter. Nevertheless, for the HERGs this parameter essentially only gives an upper limit on the bright-end slope.

3.7 Fitting the local LERG and HERG populations

In Fig. 9, we show fits of equation (4) to the local LERG and HERG populations. We add an upper-limit point to include the information from a lack of a detection at high radio luminosities. The value of the upper limit is set such that we can be 68 per cent confident the ‘true’ volume density is lower, under the assumption of a Poisson distribution (Gehrels 1986). The luminosity distributions can be well represented by this function and we summarize the best-fitting parameter values and their uncertainty in Table 3.

Table 3. Best fitted double power-law parameters for the local HERG and LERG luminosity functions.

	LERGs ($m_i < 20.5$)	HERGs ($m_i < 20.5$)	LERGs ($M_i < -23$)	HERGs ($M_i < -23$)
$\log(C)$	$-6.05^{+0.07}_{-0.07}$	$-7.87^{+0.19}_{-0.70}$	$-5.97^{+0.08}_{-0.08}$	$-7.69^{+0.16}_{-0.41}$
$\log(P^*)$	$25.21^{+0.06}_{-0.07}$	$26.47^{+1.18}_{-0.23}$	$25.08^{+0.08}_{-0.09}$	$26.38^{+1.27}_{-0.20}$
α	$-0.53^{+0.03}_{-0.07}$	$-0.66^{+0.05}_{-0.04}$	$-0.28^{+0.05}_{-0.04}$	$-0.35^{+0.09}_{-0.06}$
β	$-2.67^{+0.42}_{-0.62}$	< 0	$-0.33^{+0.08}_{-0.07}$	< 0

3.8 Redshift evolution

To examine the redshift evolution of the LERG and HERG population, we construct radio luminosity functions for each in multiple redshift bins. We present the luminosity functions in the same redshift bins as those used for the bivariate luminosity functions shown in Fig. 4. That is: $0.005 < z < 0.30$; $0.30 < z < 0.50$; and $0.5 < z < 0.75$. We restrict our analysis to $M_i < -23$; corresponding to the faintest galaxies we can detect at $z = 0.75$. They are plotted in Fig. 10. The LERG luminosity functions, shown in the left-hand panels of Fig. 10, exhibit little change in space density with increasing redshift. In contrast, the HERG luminosity functions (right-hand panels of Fig. 10) evolve more rapidly. In the highest luminosity bins, the evolution presents as a lack of detections in the lower redshift bins resulting in only upper limits on the space density of powerful radio galaxies at these redshifts.

The redshift evolution of radio galaxies is often parametrized in terms of pure luminosity evolution, where

$$L^*(z) = L^*(0)(1+z)^{K_L} \quad (7)$$

(Boyle, Shanks & Peterson 1988; Sadler et al. 2007). Substituting into equation (4) this results in a fitting function of the form

$$\Phi(L, z) = \frac{C}{\left(\frac{L^*(0)(1+z)^{K_L}}{L}\right)^\alpha + \left(\frac{L^*(0)(1+z)^{K_L}}{L}\right)^\beta}. \quad (8)$$

The other common parametrization is pure density evolution, such that

$$\Phi(z) = (1+z)^{K_D} \Phi(0) \quad (9)$$

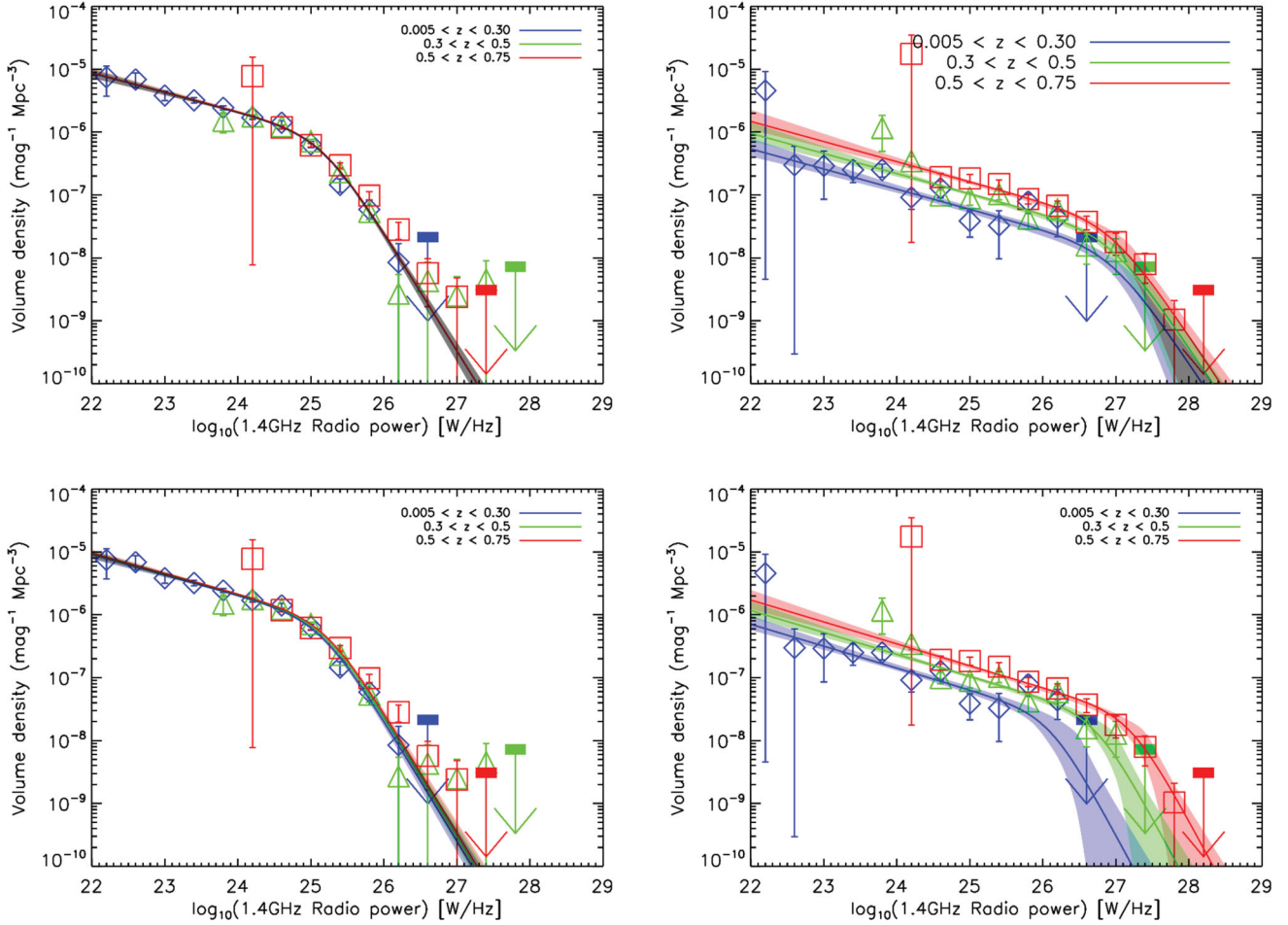


Figure 10. The radio luminosity function for LERGs (left-hand column) and HERGs (right-hand column) separated into three redshift bins: $0.005 < z < 0.30$ (blue); $0.30 < z < 0.50$ (green); $0.5 < z < 0.75$ (red). The top row shows the fit to the data (solid lines) assuming pure density evolution and the bottom row shows the fit to the data assuming pure luminosity evolution.

giving

$$\Phi(L, z) = \frac{C(1+z)^{K_D}}{(L^*/L)^\alpha + (L^*/L)^\beta}. \quad (10)$$

There is a degeneracy between luminosity and density evolution, especially when the bright population is not tightly constrained (Le Floch et al. 2005; Smolčić et al. 2009). We therefore do not fit jointly for luminosity and density evolution but restrict ourselves to the cases above.

We fitted, using a Markov Chain Monte Carlo (MCMC) method, both the LERGs (left-hand column of Fig. 10) and HERGs (right-hand column of Fig. 10) with a pure density evolution model (top row of Fig. 10) and a pure luminosity evolution model (second row of Fig. 10). The evolution in the LERGs can be well represented by either model with the pure luminosity evolution marginally preferred with difference in AIC of ~ 3.5 (equivalent to a maximum likelihood ratio of ~ 6). In the case of the HERGs, there is a similar preference for the pure density evolution model with a difference in AIC ~ 3.1 equivalent to a maximum likelihood ratio of ~ 4.5 . The best-fitting parameters and their uncertainties are summarized in Table 4. Parametrized in this way, the LERGs evolve slowly with redshift as $\sim(1+z)^{0.06^{+0.17}_{-0.18}}$ assuming pure density evolution or $\sim(1+z)^{0.46^{+0.22}_{-0.24}}$ assuming pure luminosity evolution. Under both assumptions this is consistent with no evolution within $\sim 2\sigma$. The HERGs evolve faster

Table 4. Best fitted double power-law parameters for the redshift evolution of the LERGs and HERGs.

	LERGs		HERGs	
	Density	Luminosity	Density	Luminosity
$\log(C)$	$-6.05^{+0.07}_{-0.06}$	$-6.06^{+0.06}_{-0.05}$	$-8.04^{+0.17}_{-0.24}$	$-7.59^{+0.12}_{-0.19}$
$\log(P^*)$	$25.17^{+0.06}_{-0.06}$	$25.12^{+0.06}_{-0.07}$	$26.96^{+0.27}_{-0.19}$	$25.66^{+0.40}_{-0.23}$
α	$-0.31^{+0.04}_{-0.03}$	$-0.32^{+0.04}_{-0.03}$	$-0.32^{+0.04}_{-0.05}$	$0.35^{+0.04}_{-0.05}$
β	$-1.88^{+0.10}_{-0.12}$	$-1.92^{+0.12}_{-0.11}$	$-1.75^{+0.29}_{-1.40}$	$-2.17^{+0.49}_{-4.50}$
$K_{D,L}$	$0.06^{+0.17}_{-0.18}$	$0.46^{+0.22}_{-0.24}$	$2.93^{+0.46}_{-0.47}$	$7.41^{+0.79}_{-1.33}$

than the LERGs with $\sim(1+z)^{2.93^{+0.46}_{-0.47}}$ in the pure density evolution case. If a pure luminosity evolution model is used, the parametrized redshift dependence is very rapid $\sim(1+z)^{7.41^{+0.79}_{-1.33}}$. The luminosity functions for the LERGs and the HERGs are tabulated in Tables 5 and 6.

4 DISCUSSION

It is well established that there is luminosity-dependent evolution in the overall radio AGN population, in the sense that the space density of the high luminosity population increases more rapidly with redshift (e.g. Longair 1966; Doroshkevich et al. 1970; Willott

Table 5. Luminosity function of LERGs in three redshift bins ($0.005 < z < 0.30$, $0.30 < z < 0.50$, $0.50 < z < 0.75$). Only galaxies with optical I -band absolute magnitude $M_i < -23$ are included.

$\log_{10} P_{1.4}$ (W Hz $^{-1}$)	N	$0.005 < z < 0.30$		$0.30 < z < 0.50$		$0.50 < z < 0.75$	
		$\log(\Phi)$ (mag $^{-1}$ Mpc $^{-3}$)	N	$\log(\Phi)$ (mag $^{-1}$ Mpc $^{-3}$)	N	$\log(\Phi)$ (mag $^{-1}$ Mpc $^{-3}$)	N
21.80	1	$-4.78^{+0.30}_{-3.00}$					
22.20	4	$-5.13^{+0.18}_{-0.30}$					
22.60	15	$-5.16^{+0.10}_{-0.13}$					
23.00	34	$-5.42^{+0.07}_{-0.08}$					
23.40	96	$-5.49^{+0.04}_{-0.05}$					
23.80	216	$-5.61^{+0.03}_{-0.03}$	8	$-5.82^{+0.13}_{-0.19}$			
24.20	193	$-5.77^{+0.03}_{-0.03}$	289	$-5.75^{+0.02}_{-0.03}$	1	$-5.11^{+0.30}_{-3.00}$	
24.60	163	$-5.85^{+0.03}_{-0.04}$	371	$-5.91^{+0.02}_{-0.02}$	213	$-5.93^{+0.03}_{-0.03}$	
25.00	79	$-6.19^{+0.05}_{-0.05}$	218	$-6.15^{+0.03}_{-0.03}$	242	$-6.21^{+0.03}_{-0.03}$	
25.40	17	$-6.84^{+0.09}_{-0.12}$	77	$-6.64^{+0.05}_{-0.05}$	121	$-6.53^{+0.04}_{-0.04}$	
25.80	7	$-7.23^{+0.14}_{-0.21}$	17	$-7.27^{+0.09}_{-0.12}$	45	$-7.01^{+0.06}_{-0.07}$	
26.20	1	$-8.07^{+0.30}_{-3.00}$	1	$-8.57^{+0.30}_{-3.00}$	11	$-7.55^{+0.11}_{-0.16}$	
26.60			1	$-8.36^{+0.30}_{-3.00}$	2	$-8.24^{+0.23}_{-0.53}$	
27.00			1	$-8.60^{+0.30}_{-3.00}$	1	$-8.62^{+0.30}_{-2.98}$	
27.40			1	$-8.35^{+0.30}_{-3.00}$			

Table 6. Luminosity function of HERGs in three redshift bins ($0.005 < z < 0.30$, $0.30 < z < 0.50$, $0.50 < z < 0.75$). Only galaxies with optical I -band absolute magnitude $M_i < -23$ are included.

$\log_{10} P_{1.4}$ (W Hz $^{-1}$)	N	$0.005 < z < 0.30$		$0.30 < z < 0.50$		$0.50 < z < 0.75$	
		$\log(\Phi)$ (mag $^{-1}$ Mpc $^{-3}$)	N	$\log(\Phi)$ (mag $^{-1}$ Mpc $^{-3}$)	N	$\log(\Phi)$ (mag $^{-1}$ Mpc $^{-3}$)	N
22.20	1	$-5.34^{+0.30}_{-3.00}$					
22.60	1	$-6.53^{+0.30}_{-3.00}$					
23.00	2	$-6.54^{+0.23}_{-0.53}$					
23.40	7	$-6.60^{+0.14}_{-0.21}$					
23.80	18	$-6.60^{+0.09}_{-0.12}$	3	$-5.93^{+0.20}_{-0.37}$			
24.20	8	$-7.04^{+0.13}_{-0.19}$	28	$-6.46^{+0.08}_{-0.09}$	1	$-4.76^{+0.30}_{-3.00}$	
24.60	12	$-6.89^{+0.11}_{-0.15}$	25	$-7.00^{+0.08}_{-0.10}$	47	$-6.72^{+0.06}_{-0.07}$	
25.00	5	$-7.41^{+0.16}_{-0.26}$	19	$-7.05^{+0.09}_{-0.11}$	46	$-6.74^{+0.06}_{-0.07}$	
25.40	2	$-7.48^{+0.23}_{-0.53}$	26	$-6.99^{+0.08}_{-0.09}$	42	$-6.83^{+0.06}_{-0.07}$	
25.80	8	$-7.10^{+0.13}_{-0.19}$	10	$-7.38^{+0.12}_{-0.16}$	35	$-7.06^{+0.06}_{-0.08}$	
26.20	4	$-7.36^{+0.18}_{-0.30}$	16	$-7.23^{+0.10}_{-0.12}$	30	$-7.17^{+0.07}_{-0.09}$	
26.60			4	$7.80^{+0.18}_{-0.30}$	16	$-7.43^{+0.10}_{-0.12}$	
27.00			3	$-7.89^{+0.20}_{-0.37}$	7	$-7.75^{+0.14}_{-0.21}$	
27.40					4	$-8.10^{+0.18}_{-0.30}$	
27.80					1	$-8.98^{+0.30}_{-3.02}$	

et al. 2001; Sadler et al. 2007; Smolčić et al. 2009). This differential evolution can be explained by a two-population scenario where the LERGs dominate the space density at all but the highest radio luminosity and evolve slowly with redshift, while the HERGs that dominate at the highest radio luminosities evolve more rapidly (Smolčić et al. 2009; Best & Heckman 2012; Best et al. 2014).

The expectation is that the LERGs are hosted by quiescent galaxies and powered by Bondi & Hoyle (1944) accretion from their hot gas atmospheres (e.g. Hardcastle et al. 2007; Best & Heckman 2012). In this case, a first-order prediction is that the LERGs will

evolve in a similar manner to the stellar mass function of massive quiescent galaxies. In this case, a mild decrease with increasing redshift is expected over the redshift range considered here (i.e. $z < 0.75$) evolving down in space density as $\sim(1+z)^{-0.1}$ (Best et al. 2014). In reality, the evolution will be complicated by dependence on quantities like the halo hot gas fraction and the cooling function (e.g. Croton et al. 2006) and the average density of the medium into which the radio jets are expanding (Best et al. 2014). Croton et al. (2006) predict an almost flat black hole accretion rate density over this redshift range (see Fig. 13). In any case, the expectation is we should observe little evolution in our LERG luminosity function out to $z = 0.75$, and this is the case with our best-fitting pure density evolution model evolving as $\sim(1+z)^{0.06^{+0.17}_{-0.18}}$ consistent with zero evolution. It should be noted that the evolution measured from our luminosity functions is only for the optically brightest galaxies ($M_i < -23.0$), and that our application of an e -correction means we are including the same stellar mass hosts at all redshifts. If the e -correction is not applied our luminosity functions would display a significant positive redshift evolution of the space density of $\sim(1+z)^{0.81^{+0.15}_{-0.16}}$ (assuming pure density evolution).

In this dual accretion mode picture, the HERGs are some subset of the optical quasars and Seyfert galaxies. Croom et al. (2009) measured the evolution of the QSO luminosity function in the interval $0.4 < z < 2.6$ using the 2SLAQ sample. At the lowest redshifts ($z \lesssim 1$), the number density evolves rapidly in a manner that depends on luminosity – in the sense that the brightest QSOs evolve faster. At the bright end ($M_g \sim -24$), the space density increases between their lowest redshift bins ($0.40 < z < 0.68$ and $0.68 < z < 1.06$) by a factor of ~ 3 which is similar to the change expected from our best-fitting pure density model which has space density evolving as $\sim(1+z)^{2.93}$.

We did not apply an e -correction for the HERGs when constructing the bivariate luminosity functions. Since the HERGs often have ongoing star formation and it is plausible that the AGN activity and star formation histories are related – it is inappropriate to represent them as having a stellar population which fades with time as it ages. Generally the recent star formation will contribute much of the optical light, nevertheless there will be some fading of the underlying older stellar population. Applying an e -correction will reduce the magnitude of the evolution in the luminosity function since it shifts higher redshift objects fainter and out of the selection limits. To investigate the maximum difference an e -correction could make to the evolution of the HERG luminosity function, we applied the same e -correction for the HERGs as was applied to the LERGs (which will overestimate the magnitude of the correction) and fitted for the evolution. In the pure density evolution case, we find evolution in the space density of $\sim(1+z)^{2.14^{+0.52}_{-0.63}}$. If a pure luminosity evolution model is used, the redshift dependence is $\sim(1+z)^{5.78^{+0.92}_{-2.01}}$.

A clear difference between the luminosity functions of the LERGs and the HERGs is the radio power of the turnover. The bright-end turn down in the HERG luminosity function is ~ 1 dex brighter than that of the LERGs (see e.g. Fig. 10 or Table 4). The bright-end cut-off in the i -band optical luminosity function of our HERGs and LERGs is approximately the same (see abscissa values of Fig. 6); implying, to first order, a similar cut-off in the black hole mass function of the two samples. The origin of the high power cut-off in the radio luminosity function is likely related to the cut-off in the black hole mass function modulated in some way by the accretion rate and jet-production efficiency. The Eddington scaled accretion rate in the HERGs is expected to be 1–2 dex higher than in LERGs (Best & Heckman 2012; Mingo et al. 2014; Fernandes et al. 2015;

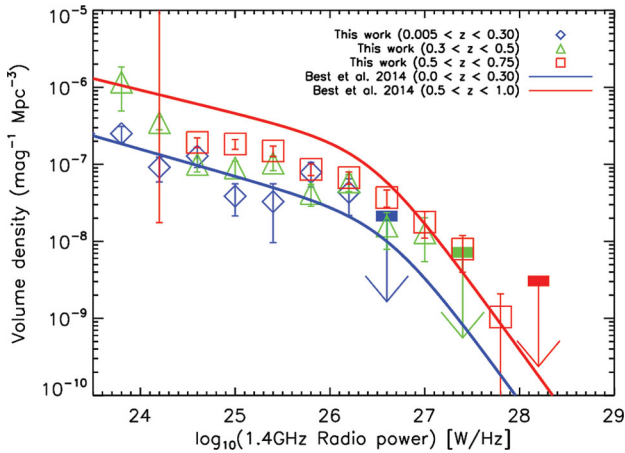


Figure 11. A comparison of the radio luminosity functions for the HERGs measured in this work (data points) and the radio luminosity functions of the HERGs from Best et al. (2014) shown as the solid lines. The three redshift intervals for our data are: $0.005 < z < 0.30$ (blue); $0.30 < z < 0.50$ (green); $0.5 < z < 0.75$ (red). Whilst Best et al. (2014) give their radio luminosity function parameters for $0.005 < z < 0.30$ (blue line) and $0.5 < z < 1.0$ (red line).

Turner & Shabala 2015). This difference should be offset to some extent by the higher jet production efficiency in the LERGs (i.e. the ratio of mechanical power to total power; Turner & Shabala in preparation). In combination, the expected mechanical power in units of the Eddington luminosity should be ~ 1 dex lower for the LERGs than the HERGs (Turner & Shabala in preparation). This is consistent with the differences in the characteristic radio power in the HERG and LERG luminosity functions, and is supportive of a picture in which these two populations are powered by different accretion modes.

4.1 Comparison with Best et al. (2014)

The only previous work on the evolution of the radio luminosity function separated by ‘accretion mode’ using optical spectroscopy was made by Best et al. (2014) using a composite sample constructed from eight different radio surveys with a range of flux density limits. This sample contains 211 radio galaxies with redshifts in the range $0.5 < z < 1.0$. As their local comparison sample they use the radio luminosity functions of Best & Heckman (2012) but with the HERGs replaced above $L_{1.4\text{GHz}} = 10^{26} \text{ W Hz}^{-1}$ with the steep spectrum radio luminosity function from the CONFIG sample (Gendre et al. 2010; Heckman & Best 2014).

4.1.1 Comparison of HERGs

The HERG radio luminosity function of Best et al. (2014) exhibits an increase in space density between the local measurement at $z < 0.3$ and their high-redshift measurement at $0.5 < z < 1.0$ of a constant factor of ~ 7 . This increase is independent of radio luminosity, and well described by pure density evolution. Our HERG radio luminosity functions are measured in three redshift bins with $z < 0.3$, $0.3 < z < 0.5$, and $0.5 < z < 0.75$. In the best-fitting pure density evolution model the space density increases as $(1+z)^{2.93+0.46}_{-0.47}$ which, if extrapolated to the upper redshift bin of Best et al. (2014) corresponds to slightly slower evolution in the space density of a factor of ~ 4 – 5 . This is illustrated in Fig. 11 where we compare the best-fitting HERG radio luminosity functions

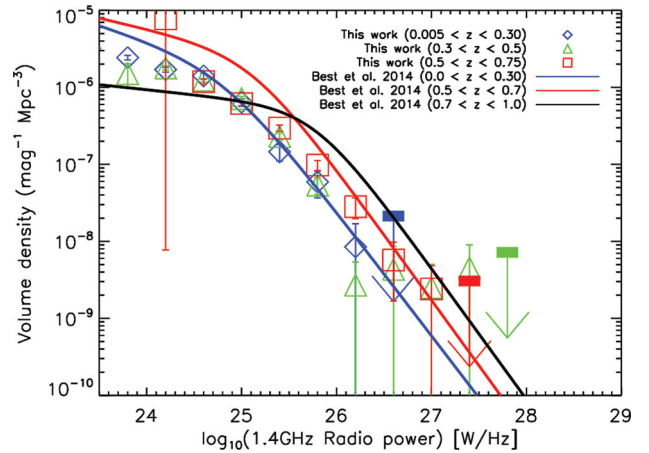


Figure 12. A comparison of the radio luminosity functions for the LERGs measured in this work (data points) and the radio luminosity functions of the ‘jet-mode’ AGN from Best et al. (2014) shown as the solid lines. The three redshift intervals for our data are: $0.005 < z < 0.30$ (blue); $0.30 < z < 0.50$ (green); $0.5 < z < 0.75$ (red). Whilst Best et al. (2014) give their radio luminosity function parameters for the LERGs at $0.005 < z < 0.30$ (blue line), $0.5 < z < 0.7$ (red line) and $0.7 < z < 1.0$ (black line).

of Best et al. (2014) with our HERG radio luminosity function data. This comparison is not quantitatively precise since the classification scheme, and redshift ranges are not identical. The high redshift bin of Best et al. (2014) is $0.5 < z < 1.0$ (red line), whereas our highest redshift bin is $0.5 < z < 0.75$. Furthermore, we only included the brightest optical galaxies ($M_i < -23.0$) when fitting for the redshift evolution. If the faint-optical population evolves more rapidly than this would increase the redshift evolution of the space density.

4.1.2 Comparison of LERGs

For the LERGs, Best et al. (2014) do find luminosity-dependent evolution in the radio luminosity function. At low radio luminosities ($L_{1.4\text{GHz}} = 10^{25} \text{ W Hz}^{-1}$) they find the space density is nearly constant or increases slowly out to $z \sim 0.5$ – 0.7 and then begins to decrease out to $z = 1$. At high radio luminosity they measure a more rapid increase in space density of LERGs with redshift, rising by a factor of ~ 10 for the highest radio luminosities. In contrast, we measure much slower evolution in the LERG luminosity function consistent with zero at less than $\sim 2\sigma$ for both the pure density and pure luminosity evolution models. We do find that the luminosity evolution model is a better fit to the data but this preference is marginal.

These differences, however, are not as significant as they seem since much of the complexity in the evolution seen by Best et al. (2014) occurs in their highest redshift bin ($0.7 < z < 1.0$). In Fig. 12, we compare our radio luminosity function data points with the best-fitting models of Best et al. (2014). They are in generally good agreement when comparing the low redshift bins ($z < 0.3$) and our high redshift bin ($0.5 < z < 0.75$) with their intermediate redshift bin ($0.5 < z < 0.7$). The main difference being Best et al. (2014) measure a higher space density (a factor of ~ 2 – 5) of low-luminosity LERGs at both redshifts. We do see the beginning of a decrease in space density of the faintest sources with increasing redshift, i.e. at faint radio luminosities ($L_{1.4\text{GHz}} \lesssim 10^{25.5} \text{ W Hz}^{-1}$) the density measured in our intermediate redshift bin is higher than in the highest redshift bin. Best et al. (2014) propose one possible explanation for this decrease as: the space density evolving in line

with the density of massive quiescent galaxies and a time delay between the onset of the radio AGN after the formation of the quiescent host galaxy.

As pointed out earlier, when considering redshift evolution, samples with the same optical brightness constraints should be used otherwise different fractions of the total population will be counted at different redshifts. Best et al. (2014) do not apply such a constraint instead mitigating such effects by only including surveys with high redshift completeness in their sample. For example, at a completeness of unity all radio sources are counted and there will be no optical selection effects. Best et al. (2014) do not state their spectroscopic completeness values for all eight of the radio surveys used in their combined sample, however, in several cases they restrict their flux density ranges to ensure completeness. We, however, only include the optically brightest galaxies in our sample ($M_i < -23$) which has the effect of decreasing the normalization of the luminosity function. We have already demonstrated that when we do not restrict our sample to $M_i < -23$ our local LERG luminosity function agrees with that of Best et al. (2014, see Fig. 5).

4.2 Radio-mode feedback

There is substantial evidence that radio jets from LERGs are important in regulating star formation in massive galaxies and clusters of galaxies by injecting energy into the hot gas atmosphere and inhibiting gas cooling and star formation. This radio-mode AGN feedback can simultaneously explain the ‘cooling flow problem’, the exponential cut-off in the bright end of the optical galaxy luminosity function and the old stellar populations of the most massive bulges (e.g. Bower et al. 2006; Croton et al. 2006). Estimates of the energy associated with bubbles and cavities in the intergalactic medium surrounding elliptical galaxies and galaxy clusters can be used to estimate the mechanical power associated with the radio jets producing the cavities. The empirical correlation of these energies with monochromatic radio luminosity can be used to transform between the two (Dunn, Fabian & Taylor 2005; Rafferty et al. 2006; Birzan et al. 2008; Cavagnolo et al. 2010). Although, these relations have large intrinsic scatter of ~ 0.7 dex (Cavagnolo et al. 2010). Using such relations the monochromatic radio luminosity function

can be transformed into a mechanical power density function, and integrated to calculate the total mechanical power (per unit volume) available for radio-mode feedback (e.g. Best et al. 2006; Smolčić et al. 2009). That is, we calculate

$$\int \phi(P_m) P_m d(0.4 \log_{10} P_m) = \frac{2.5}{\ln(10)} \int \phi(P_m) dP_m \quad (11)$$

where P_m is the mechanical power which we calculate from the 1.4 GHz luminosity using equation 1 of Cavagnolo et al. (2010). The factor of $2.5/\ln(10)$ comes about since our luminosity function is in units of mag^{-1} rather than units of the natural logarithm.

In Fig. 13, we show this integral as a function of redshift using our pure density evolution fits to the LERGs and HERGs. We follow Smolčić et al. (2009) and integrate above a mechanical power equivalent to $L_{1.4\text{GHz}} = 10^{21} \text{ W Hz}^{-1}$. The shaded regions illustrate the uncertainties from the conversion of 1.4 GHz radio luminosity to mechanical power using the uncertainties quoted in Cavagnolo et al. (2010, equation 1) (large shaded regions), and from the uncertainties in our parameter values from fitting the radio luminosity function; constructed by sampling the posterior distribution of the parameters obtained from the MCMC fitting (smaller dark shaded regions).

There is little evolution with redshift in the volume density of mechanical power from the LERGs (*left-hand panel* of Fig. 13), consistent with the prediction from the cosmological model of Croton et al. (2006); shown as the dashed line. It should be noted these mechanical powers only include emission from massive galaxies since our radio luminosity functions are restricted to $M_i < -23$, including fainter optical galaxies will increase the normalization further. Also, in the left-hand panel of Fig. 13 we show the mechanical power calculated from fits to the radio luminosity function of low-luminosity VLA-COSMOS AGN (Smolčić et al. 2009). The low-luminosity selection means the radio luminosity function should be dominated by LERGs although it will still contain a contribution from the HERGs. The normalization of our estimate of the total mechanical power is a factor of ~ 4 lower than that measured by Smolčić et al. (2009). This difference can be attributed to our restriction to only the very brightest optical galaxies ($M_i < -23$) causing the normalization of our luminosity functions to be

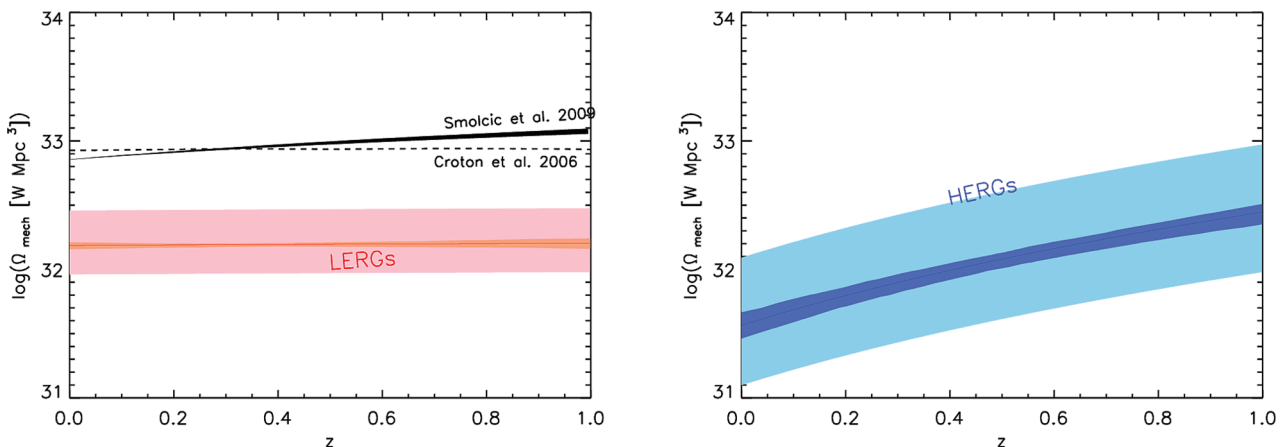


Figure 13. The total mechanical power per unit volume as function of redshift estimated from the pure density evolution fits to our radio luminosity functions. The conversion to mechanical power from 1.4 GHz luminosity uses the relation of Cavagnolo et al. (2010). The shaded regions represent the uncertainty from the radio luminosity function fits (smaller dark shaded regions) and the uncertainty in the Cavagnolo et al. (2010) relation (the larger shaded regions). The left-hand panel is for the LERGs and the right-hand panel is for the HERGs. Also overplotted on the LERGs are the prediction from the cosmological model of Croton et al. (2006) and the measurement from Smolčić et al. (2009). The difference in normalization between our measurement and that of Smolčić et al. (2009) can be entirely attributed to our measurement only including the contribution from the brightest optical galaxies (see text for details).

lower. The difference in normalization of the luminosity functions accounts for all of this factor of 4 (cf. our Fig. 10 with Smolčić et al. 2009 fig. 3). We also show the evolution of the mechanical power calculated for the HERGs (*right-hand panel*). The normalization of this is approximately an order of magnitude smaller than that of the LERGs at $z = 0$ but becomes comparable at $z = 1$. Since the measurement of Smolčić et al. (2009) includes both HERGs and LERGs, this evolution in the HERGs can account for their factor of ~ 2 evolution in the total mechanical power out to $z = 1$.

5 SUMMARY

We have constructed radio luminosity functions out to a redshift of $z = 0.75$ using a new sample of 5026 radio galaxies with 1.4 GHz flux density: $S_{1.4\text{GHz}} > 2.8$ mJy and optical magnitude: $m_i < 20.5$ mag. These radio galaxies have confirmed spectroscopic redshifts. The optical spectra are also used to classify the radio galaxies as star forming or AGN. The AGN are further subdivided into HERGs or LERGs. Using a subset of the brightest optical galaxies with $M_i < -23$, we characterize the evolution in the radio luminosity function of these objects. We find the following.

(i) The space density of the LERGs exhibits little evolution with redshift. The LERGs evolve as $\sim(1+z)^{0.06^{+0.17}_{-0.18}}$ under the assumption of pure density evolution or $\sim(1+z)^{0.46^{+0.22}_{-0.24}}$ under the assumption of pure luminosity evolution. Both are consistent with zero evolution at less than 2σ . Since the LERGs dominate the number density of radio AGN at low radio luminosity, this result is consistent with the mild evolution seen in the total radio luminosity function at low radio power.

(ii) The HERGs evolve more rapidly best fitted by $\sim(1+z)^{2.93^{+0.46}_{-0.47}}$ assuming pure density evolution or $\sim(1+z)^{7.41^{+0.79}_{-1.33}}$ under the pure luminosity evolution assumption. Since the HERGs dominate the space density at only the highest luminosities, this is consistent with the more rapid evolution of bright radio galaxies observed in the overall radio AGN population.

(iii) The bright-end turn down in the radio luminosity function occurs at a significantly higher power ($\gtrsim 1$ dex) for the HERG population than the LERG population. This is consistent with the two populations representing fundamentally different accretion modes.

(iv) Converting the LERG luminosity function to a mechanical power density function using empirical relations and integrating, results in a total mechanical power per unit volume available for radio-mode feedback that remains roughly constant out to $z = 0.75$. This is consistent with cosmological models.

ACKNOWLEDGEMENTS

We are grateful to the anonymous referee for insightful comments which greatly improved this paper.

EMS and SMC acknowledge the financial support of the Australian Research Council through Discovery Project grants DP1093086 and DP 130103198. SMC acknowledges the support of an Australian Research Council Future Fellowship (FT100100457). SB acknowledges the funding support from the Australian Research Council through a Future Fellowship (FT140101166).

Funding for the SDSS and SDSS-II has been provided by the Alfred P. Sloan Foundation, the Participating Institutions, the National Science Foundation, the US Department of Energy, the National Aeronautics and Space Administration, the Japanese Monbukagakusho, and the Max Planck Society, and the Higher

Education Funding Council for England. The SDSS website is <http://www.sdss.org/>.

The SDSS is managed by the Astrophysical Research Consortium (ARC) for the Participating Institutions. The Participating Institutions are the American Museum of Natural History, Astrophysical Institute Potsdam, University of Basel, University of Cambridge, Case Western Reserve University, The University of Chicago, Drexel University, Fermilab, the Institute for Advanced Study, the Japan Participation Group, The Johns Hopkins University, the Joint Institute for Nuclear Astrophysics, the Kavli Institute for Particle Astrophysics and Cosmology, the Korean Scientist Group, the Chinese Academy of Sciences (LAMOST), Los Alamos National Laboratory, the Max-Planck-Institute for Astronomy (MPIA), the Max-Planck-Institute for Astrophysics (MPA), New Mexico State University, Ohio State University, University of Pittsburgh, University of Portsmouth, Princeton University, the United States Naval Observatory and the University of Washington.

The WiggleZ project wishes to acknowledge financial support from The Australian Research Council (grants DP0772084 and LX0881951 directly for the WiggleZ project, and grant LE0668442 for programming support).

GALEX is a NASA small explorer, launched in 2003 April. We gratefully acknowledge NASA's support for construction, operation and science analysis for the *GALEX* mission, developed in cooperation with the Centre National d'études Spatiales of France and the Korean Ministry of Science and Technology.

GAMA is a joint European–Australian project based around a spectroscopic campaign using the Anglo-Australian Telescope. The GAMA input catalogue is based on data taken from the SDSS and the UKIRT Infrared Deep Sky Survey. Complementary imaging of the GAMA regions is being obtained by a number of independent survey programmes including *GALEX* MIS, VST KIDS, VISTA VIKING, *WISE*, *Herschel*-ATLAS, GMRT and ASKAP providing UV to radio coverage. GAMA is funded by the STFC (UK), the ARC (Australia), the AAO, and the participating institutions. The GAMA website is <http://www.gama-survey.org/>.

REFERENCES

- Adelman-McCarthy J. K. et al., 2008, *ApJS*, 175, 297
 Akaike H., 1974, *IEEE Trans. Autom. Control*, 19, 716
 Antonucci R., 1993, *ARA&A*, 31, 473
 Baldry I. K. et al., 2010, *MNRAS*, 404, 86
 Baldwin J. A., Phillips M. M., Terlevich R., 1981, *PASP*, 93, 5 (BPT)
 Becker R. H., White R. L., Helfand D. J., 1995, *ApJ*, 450, 559
 Best P. N., Heckman T. M., 2012, *MNRAS*, 421, 1569
 Best P. N., Kauffmann G., Heckman T. M., Brinchmann J., Charlot S., Ivezić Ž., White S. D. M., 2005, *MNRAS*, 362, 25
 Best P. N., Kaiser C. R., Heckman T. M., Kauffmann G., 2006, *MNRAS*, 368, L67
 Best P. N., Ker L. M., Simpson C., Rigby E. E., Sabater J., 2014, *MNRAS*, 445, 955
 Binney J., Tabor G., 1995, *MNRAS*, 276, 663
 Bîrzan L., McNamara B. R., Nulsen P. E. J., Carilli C. L., Wise M. W., 2008, *ApJ*, 686, 859
 Blanton M. R., Roweis S., 2007, *AJ*, 133, 734
 Bondi H., Hoyle F., 1944, *MNRAS*, 104, 273
 Bower R. G., Benson A. J., Malbon R., Helly J. C., Frenk C. S., Baugh C. M., Cole S., Lacey C. G., 2006, *MNRAS*, 370, 645
 Boyle B. J., Shanks T., Peterson B. A., 1988, *MNRAS*, 235, 935
 Brown M. J. I., Webster R. L., Boyle B. J., 2001, *AJ*, 121, 2381
 Cannon R. et al., 2006, *MNRAS*, 372, 425
 Cavagnolo K. W., McNamara B. R., Nulsen P. E. J., Carilli C. L., Jones C., Bîrzan L., 2010, *ApJ*, 720, 1066

- Chiaberge M., Macchetto F. D., Sparks W. B., Capetti A., Allen M. G., Martel A. R., 2002, *ApJ*, 571, 247
- Ching J., 2015, PhD thesis, Sydney Univ.
- Cirasuolo M., Magliocchetti M., Gentile G., Celotti A., Cristiani S., Danese L., 2006, *MNRAS*, 371, 695
- Clewley L., Jarvis M. J., 2004, *MNRAS*, 352, 909
- Condon J. J., Cotton W. D., Greisen E. W., Yin Q. F., Perley R. A., Taylor G. B., Broderick J. J., 1998, *AJ*, 115, 1693
- Condon J. J., Cotton W. D., Broderick J. J., 2002, *AJ*, 124, 675
- Croom S. M., Smith R. J., Boyle B. J., Shanks T., Miller L., Outram P. J., Loaring N. S., 2004, *MNRAS*, 349, 1397
- Croom S. M. et al., 2009, *MNRAS*, 392, 19
- Croton D. J. et al., 2006, *MNRAS*, 365, 11
- Davis T. A. et al., 2012, *MNRAS*, 426, 1574
- Donoso E., Best P. N., Kauffmann G., 2009, *MNRAS*, 392, 617
- Doroshkevich A. G., Longair M. S., Zeldovich Y. B., 1970, *MNRAS*, 147, 139
- Drinkwater M. J. et al., 2010, *MNRAS*, 401, 1429
- Driver S. P. et al., 2011, *MNRAS*, 413, 971
- Dunlop J. S., Peacock J. A., 1990, *MNRAS*, 247, 19
- Dunn R. J. H., Fabian A. C., Taylor G. B., 2005, *MNRAS*, 364, 1343
- Fabian A. C., Celotti A., Blundell K. M., Kassim N. E., Perley R. A., 2002, *MNRAS*, 331, 369
- Fernandes C. A. C. et al., 2015, *MNRAS*, 447, 1184
- Ganguly R., Brotherton M. S., 2008, *ApJ*, 672, 102
- Gebhardt K. et al., 2000, *ApJ*, 539, L13
- Gehrels N., 1986, *ApJ*, 303, 336
- Gendre M. A., Best P. N., Wall J. V., 2010, *MNRAS*, 404, 1719
- Hardcastle M. J., Evans D. A., Croston J. H., 2007, *MNRAS*, 376, 1849
- Harrison C. M., Alexander D. M., Mullaney J. R., Swinbank A. M., 2014, *MNRAS*, 441, 3306
- Heckman T. M., Best P. N., 2014, *ARA&A*, 52, 589
- Herbert P. D., Jarvis M. J., Willott C. J., McLure R. J., Mitchell E., Rawlings S., Hill G. J., Dunlop J. S., 2010, *MNRAS*, 406, 1841
- Hill G. J., Rawlings S., 2003, *New Astron. Rev.*, 47, 373
- Hine R. G., Longair M. S., 1979, *MNRAS*, 188, 111
- Ivezić Ž. et al., 2002, *AJ*, 124, 2364
- Jackson N., Rawlings S., 1997, *MNRAS*, 286, 241
- Jackson C. A., Wall J. V., 1999, *MNRAS*, 304, 160
- Kauffmann G. et al., 2003, *MNRAS*, 346, 1055
- Kauffmann G., Heckman T. M., Best P. N., 2008, *MNRAS*, 384, 953
- Lacy M., Rawlings S., Hill G. J., Bunker A. J., Ridgway S. E., Stern D., 1999, *MNRAS*, 308, 1096
- Laing R. A., Jenkins C. R., Wall J. V., Unger S. W., 1994, in Bicknell G. V., Dopita M. A., Quinn P. J., eds, *ASP Conf. Ser. Vol. 54, The Physics of Active Galaxies*. Astron. Soc. Pac., San Francisco, p. 201
- Le Floch E., Papovich C., Dole H., Bell E. F., Lagache G., 2005, *ApJ*, 632, 169
- Liske J. et al., 2015, *MNRAS*, 452, 2087
- Longair M. S., 1966, *MNRAS*, 133, 421
- McAlpine K., Jarvis M. J., Bonfield D. G., 2013, *MNRAS*, 436, 1084
- McElroy R., Croom S. M., Pracy M., Sharp R., Ho I.-T., Medling A. M., 2015, *MNRAS*, 446, 2186
- Machalski J., Godlowski W., 2000, *A&A*, 360, 463
- McNamara B. R., Nulsen P. E. J., 2007, *ARA&A*, 45, 117
- Magorrian J. et al., 1998, *AJ*, 115, 2285
- Mao M. Y. et al., 2012, *MNRAS*, 426, 3334
- Mauch T., Sadler E. M., 2007, *MNRAS*, 375, 931
- Mingo B., Hardcastle M. J., Croston J. H., Dicken D., Evans D. A., Morganti R., Tadhunter C., 2014, *MNRAS*, 440, 269
- Page M. J. et al., 2012, *Nature*, 485, 213
- Peacock J. A., 1985, *MNRAS*, 217, 601
- Poggianti B. M., 1997, *A&AS*, 122, 399
- Rafferty D. A., McNamara B. R., Nulsen P. E. J., Wise M. W., 2006, *ApJ*, 652, 216
- Rigby E. E., Best P. N., Brookes M. H., Peacock J. A., Dunlop J. S., Röttgering H. J. A., Wall J. V., Ker L., 2011, *MNRAS*, 416, 1900
- Sadler E. M. et al., 2002, *MNRAS*, 329, 227
- Sadler E. M. et al., 2007, *MNRAS*, 381, 211
- Saunders W., Rowan-Robinson M., Lawrence A., Efstathiou G., Kaiser N., Ellis R. S., Frenk C. S., 1990, *MNRAS*, 242, 318
- Schechter P., 1976, *ApJ*, 203, 297
- Schmidt M., 1968, *ApJ*, 151, 393
- Shabala S. S., Kaviraj S., Silk J., 2011, *MNRAS*, 413, 2815
- Silk J., Nusser A., 2010, *ApJ*, 725, 556
- Simpson C. et al., 2006, *MNRAS*, 372, 741
- Smith E. P., Heckman T. M., 1989, *ApJ*, 341, 658
- Smolčić V. et al., 2009, *ApJ*, 696, 24
- Turner R. J., Shabala S. S., 2015, *ApJ*, 809, 59
- Waddington I., Dunlop J. S., Peacock J. A., Windhorst R. A., 2001, *MNRAS*, 328, 882
- Wall J. V., Peacock J. A., 1985, *MNRAS*, 216, 173
- Whysong D., Antonucci R., 2004, *ApJ*, 602, 116
- Willott C. J., Rawlings S., Blundell K. M., Lacy M., Eales S. A., 2001, *MNRAS*, 322, 536

This paper has been typeset from a $\text{\TeX}/\text{\LaTeX}$ file prepared by the author.